Nonlinearity of Ocean Carbon Cycle Feedbacks in CMIP5 Earth System Models

Jörg Schwinger, Jerry Tjiputra, Christoph Heinze, Laurent Bopp, James Christian, Marion Gehlen, Tatiana Ilyina, Chris Jones, David Salas-Mélia, Joachim Segschneider, et al.

SPECIAL C4MIP COLLECTION

Nonlinearity of Ocean Carbon Cycle Feedbacks in CMIP5 Earth System Models

JÖRG SCHWINGER,* JERRY F. TJIPUTRA,+ CHRISTOPH HEINZE,# LAURENT BOPP,@ JAMES R. CHRISTIAN,& MARION GEHLEN,@ TATIANA ILYINA,** CHRIS D. JONES,++ DAVID SALAS-MÉLIA,## JOACHIM SEGSCHNEIDER,** ROLAND SÉFÉRIAN,@@ AND IAN TOTTERDELL++

* *Geophysical Institute, University of Bergen, and Bjerknes Centre for Climate Research, Bergen, Norway*
+ *Uni Climate, Uni Research AS, and Bjerknes Centre for Climate Research, Bergen, Norway*
# *Geophysical Institute, University of Bergen, and Bjerknes Centre for Climate Research, and Uni Climate, Uni Research AS, Bergen, Norway*
@ *Laboratoire des Sciences du Climat et de l'Environnement, Gif sur Yvette, France*
& *Canadian Centre for Climate Modelling and Analysis, Victoria, British Columbia, Canada*
** *Max Planck Institute for Meteorology, Hamburg, Germany*
++ *Met Office Hadley Centre, Exeter, United Kingdom*
Centre National de Recherches Météorologiques, Météo-France, Toulouse, France
@@ *Laboratoire des Sciences du Climat et de l'Environnement, Gif sur Yvette, and Centre National de Recherches Météorologiques, Météo-France, Toulouse, France*

(Manuscript received 25 July 2013, in final form 8 February 2014)

ABSTRACT

Carbon cycle feedbacks are usually categorized into carbon–concentration and carbon–climate feedbacks, which arise owing to increasing atmospheric CO_2 concentration and changing physical climate. Both feedbacks are often assumed to operate independently: that is, the total feedback can be expressed as the sum of two independent carbon fluxes that are functions of atmospheric CO_2 and climate change, respectively. For phase 5 of the Coupled Model Intercomparison Project (CMIP5), radiatively and biogeochemically coupled simulations have been undertaken to better understand carbon cycle feedback processes. Results show that the sum of total ocean carbon uptake in the radiatively and biogeochemically coupled experiments is consistently larger by 19–58 petagrams of carbon (Pg C) than the uptake found in the fully coupled model runs. This nonlinearity is small compared to the total ocean carbon uptake (533–676 Pg C), but it is of the same order as the carbon–climate feedback. The weakening of ocean circulation and mixing with climate change makes the largest contribution to the nonlinear carbon cycle response since carbon transport to depth is suppressed in the fully relative to the biogeochemically coupled simulations, while the radiatively coupled experiment mainly measures the loss of near-surface carbon owing to warming of the ocean. Sea ice retreat and seawater carbon chemistry contribute less to the simulated nonlinearity. The authors' results indicate that estimates of the ocean carbon–climate feedback derived from "warming only" (radiatively coupled) simulations may underestimate the reduction of ocean carbon uptake in a warm climate high CO_2 world.

1. Introduction

It is estimated that, at present, the world's oceans take up approximately 25% of anthropogenic CO_2 emissions (Le Quéré et al. 2013), thereby reducing the atmospheric CO_2 burden. At the same time, climate change modifies ocean circulation and the physical and chemical properties of seawater, which in turn can alter CO_2 uptake. These CO_2 and climate-driven effects are referred to as carbon–concentration and carbon–climate feedback (Boer and Arora 2009; Gregory et al. 2009). The first attempts to quantify these feedbacks were made decades ago (e.g., Eriksson 1963; Siegenthaler and Oeschger 1978), and the first three-dimensional atmosphere–ocean modeling experiments including both the carbon–concentration and the carbon–climate feedback were devised by Maier-Reimer et al. (1996), Sarmiento and Le Quéré (1996), and

Denotes Open Access content.

Corresponding author address: Jörg Schwinger, Geophysical Institute, Allégaten 70, 5007 Bergen, Norway.
E-mail: jorg.schwinger@gfi.uib.no

DOI: 10.1175/JCLI-D-13-00452.1

Matear and Hirst (1999). With the advent of earth system models with fully coupled land and ocean carbon cycle modules, it became possible to perform climate projections including these carbon cycle feedback mechanisms in a fully consistent manner (Cox et al. 2000; Dufresne et al. 2002; Friedlingstein et al. 2003). The first coordinated effort to estimate the magnitude of the carbon cycle feedbacks together with their uncertainties based on multiple earth system models was the Coupled Climate–Carbon Cycle Model Intercomparison Project (C^4MIP) by Friedlingstein et al. (2006) using seven ocean–atmosphere general circulation models and four earth system models of intermediate complexity (EMICs). Next to fully coupled climate–carbon cycle simulations (COU), these studies employed biogeochemically coupled model experiments (BGC) where the increasing CO_2 concentration is not "seen" by the radiation code of the model. Since there is little physical climate change in these experiments, the carbon uptake is taken to represent the carbon–concentration feedback. Further, by considering the difference between the COU and BGC model runs, it is possible to estimate the carbon–climate feedback.

Gregory et al. (2009), Tjiputra et al. (2010), Boer and Arora (2013), and Arora et al. (2013) employ radiatively coupled simulations (RAD) with constant preindustrial CO_2 concentration prescribed to the land and ocean biogeochemistry modules while the model's radiation code sees rising atmospheric CO_2. The change in carbon uptake (actually a loss) from this type of simulation is an alternative estimate of the carbon–climate feedback; likewise, it is possible to derive the carbon–concentration feedback by taking the difference from the fully coupled simulation. Gregory et al. (2009) found that the accumulated carbon fluxes simulated in the BGC and RAD experiments do not add up to the carbon flux occurring in the COU simulation in the third climate configuration of the Met Office Unified Model in lower resolution with carbon cycle (HadCM3LC). A similar result is found by Zickfeld et al. (2011), who used an EMIC [the University of Victoria (UVic) ESCM] to investigate the nonlinearity of the carbon cycle feedback on a 500-yr time scale. For the ocean, the latter authors found that the weakening of ocean circulation and increased stratification under climate change is responsible for a large part of the simulated nonlinearity since these changes have a different effect on ocean carbon uptake depending on whether atmospheric CO_2 is rising. They also attributed a part of the nonlinearity to sea ice retreat in the Southern Ocean.

In the framework of phase 5 of the Coupled Model Intercomparison Project (CMIP5) (Taylor et al. 2012), a set of fully, biogeochemically, and radiatively coupled simulations has been performed with a number of earth system models (see Table 1 for a list of the CMIP5 models). Authors of previous studies (Plattner et al. 2008; Gregory et al. 2009; Zickfeld et al. 2011) recommended employing concentration-driven rather than emission-driven scenarios for model intercomparison studies of carbon cycle processes. Therefore, in contrast to C^4MIP, CMIP5 prioritizes concentration-driven scenarios for carbon cycle feedback experiments. A standard idealized experiment with a prescribed 1% yr^{-1} increase of atmospheric CO_2 (until quadrupling of atmospheric CO_2 is reached after 140 yr) serves as a baseline simulation (COU); correspondingly, a 1% yr^{-1} increase of CO_2 is only seen by the biogeochemistry modules or the radiation code in the BGC and RAD experiments, respectively. Technically, there is no carbon cycle feedback in concentration-driven simulations since changes in the amount of carbon stored in the ocean and on land do not influence the atmospheric CO_2 concentration. Nevertheless, carbon cycle feedbacks can be diagnosed from concentration-driven experiments by analyzing the implied emissions or the changes in air–sea and air–land carbon fluxes and associated changes in carbon inventories. The feedback gain of the carbon cycle can be derived from these diagnosed inventory changes (Plattner et al. 2008; Gregory et al. 2009).

Carbon cycle feedbacks in CMIP5 earth system models for the 1% CO_2 scenario have been quantified by Arora et al. (2013) for land and ocean. No attempt was made by Arora et al., however, to exploit the available experiments with regard to nonlinearities. The aim of this study is to investigate and quantify the nonlinearity of ocean carbon cycle feedbacks found in the CMIP5 earth system models using the radiatively and biogeochemically coupled simulations. This paper is organized as follows. We employ the carbon cycle feedback metrics introduced by Friedlingstein et al. (2003) to define linear and nonlinear carbon cycle feedbacks and to derive some basic properties of the BGC, RAD, and COU experiments in section 2. The experiments and our analysis methods are described in section 3. Section 4 focuses on analyzing the contributions of the nonlinear seawater carbon chemistry, sea ice retreat, and reduced overturning and mixing to the nonlinearity of ocean carbon cycle feedbacks. A summary of results and conclusions can be found in section 5.

2. Linear and nonlinear carbon cycle feedbacks

The basic equation describing a linear carbon cycle feedback (e.g., Friedlingstein et al. 2003, 2006; Gregory et al. 2009) reads

$$\Delta C = \beta \Delta CO_2 + \gamma \Delta T, \tag{1}$$

where ΔCO_2 and ΔT denote atmospheric CO_2 and near-surface temperature deviations from the preindustrial

TABLE 1. Participating CMIP5 earth system models.

Model acronym	Model name	Modeling group	Reference	Ocean biogeochemistry model
MPI-ESM-LR	Max Planck Institute Earth System Model, low resolution	Max Planck Institute for Meteorology	Giorgetta et al. (2013)	Hamburg Oceanic Carbon Cycle (HAMOCC; Ilyina et al. 2013)
IPSL-CM5A-LR	L'Institut Pierre-Simon Laplace Coupled Model, version 5A, low resolution	L'Institut Pierre-Simon Laplace	Dufresne et al. (2013)	Pelagic Interaction Scheme for Carbon and Ecosystem Studies (PISCES; Aumont and Bopp 2006)
NorESM1-ME	Norwegian Earth System Model, version 1 (intermediate resolution)	Norwegian Climate Centre	Tjiputra et al. (2013)	HAMOCC (Assmann et al. 2010; Ilyina et al. 2013)
HadGEM2-ES	Hadley Centre Global Environment Model, version 2–Earth System	Met Office Hadley Centre	Collins et al. (2011)	Diatom version of the Hadley Centre Ocean Carbon Cycle model (Diat-HadOCC; I. Totterdell and P. Halloran 2013, unpublished manuscript; Palmer and Totterdell 2001)
CanESM2	Second Generation Canadian Earth System Model	Canadian Centre for Climate Modelling and Analysis	Arora et al. (2011)	Canadian Model of Ocean Carbon (CMOC; Zahariev et al. 2008)
CESM1(BGC)	Community Earth System Model, version 1–Biogeochemistry	Community Earth System Model Contributors	Long et al. (2013)	Biogeochemical Elemental Cycle (BEC; Moore et al. 2013)
CNRM-CM5.2	Centre National de Recherches Météorologiques Coupled Global Climate Model, version 5.2	Centre National de Recherches Météorologiques/Centre Européen de Recherche et Formation Avancée en Calcul Scientifique	Voldoire et al. (2013)	PISCES (Aumont and Bopp 2006)

state and ΔC is the resulting change in the carbon stock of one compartment of the earth system (here, the ocean). The feedback parameters β and γ have units petagrams of carbon per parts per million (Pg C ppm^{-1}) and petagrams of carbon per kelvin (Pg C K^{-1}), respectively, and are defined for land and ocean separately. Since we focus on the ocean in this study, the coefficients β and γ refer to changes in the ocean carbon inventory in the following text.

According to (1), the carbon cycle feedback consists of a carbon–concentration feedback $\beta\Delta\text{CO}_2$ and a carbon–climate feedback $\gamma\Delta T$. The formulation of the carbon–climate feedback is based on the assumption that a change of the global mean near-surface temperature T is a simple yet suitable proxy for climate change. We note that an alternative feedback formulation was introduced by Boer and Arora (2009), which has the same form as (1) but links the instantaneous carbon flux change (instead of the time-integrated flux change ΔC) to ΔCO_2 and ΔT through feedback parameters B and Γ. None of these two feedback equations includes an explicit time dependence of the system response: that is, the carbon stocks or fluxes are assumed to balance immediately with new values of CO_2 and T. Since, for our purposes, it is more convenient to use integrated quantities, that is, changes in the total ocean carbon stock, we stick to the Friedlingstein et al. (2006) approach for this study. However, the considerations that follow in this section also apply to the Boer and Arora (2009) definition of feedback parameters.

The carbon cycle feedback in (1) can be derived based on a Taylor series expansion using a number of simplifying assumptions. The basic assumption is that the carbon stock C in one compartment of the earth system (here, the ocean) can be expressed as a function of climate system state (characterized by global mean near-surface temperature) and atmospheric carbon dioxide concentration, $C = F(\text{CO}_2, T)$. Hence, deviations from the preindustrial state can be approximated by expanding F into a Taylor series:

$$\begin{aligned}\Delta C &= F(\text{CO}_{2,0} + \Delta\text{CO}_2, T_0 + \Delta T)\\ &= \left.\frac{\partial F}{\partial \text{CO}_2}\right|_0 \Delta\text{CO}_2 + \left.\frac{\partial F}{\partial T}\right|_0 \Delta T + \left.\frac{\partial^2 F}{\partial \text{CO}_2 \partial T}\right|_0 \Delta\text{CO}_2 \Delta T\\ &\quad + \frac{1}{2}\left.\frac{\partial^2 F}{\partial \text{CO}_2^2}\right|_0 \Delta\text{CO}_2^2 + \frac{1}{2}\left.\frac{\partial^2 F}{\partial T^2}\right|_0 \Delta T^2 + R_3 .\end{aligned} \tag{2}$$

Here, R_3 is the remainder term containing third-order and higher derivatives. The derivatives are taken at the preindustrial values of T and CO_2 as indicated by the subscript 0. An implicit assumption behind (2) is that the carbon cycle is in equilibrium at preindustrial state, which might not be the case for the model simulations used in this study. Therefore, all model results presented here are taken relative to a preindustrial control run.

If all second- or higher-order terms in (2) are small enough to be neglected, the carbon cycle feedback is linear, and we arrive at (1),

$$\Delta C = \Delta C_{\mathrm{CO2}} + \Delta C_{\mathrm{clim}},$$

where

$$\Delta C_{\mathrm{CO2}} = \left.\frac{\partial F}{\partial \mathrm{CO}_2}\right|_0 \Delta \mathrm{CO}_2 = \beta \Delta \mathrm{CO}_2, \quad \text{and}$$

$$\Delta C_{\mathrm{clim}} = \left.\frac{\partial F}{\partial T}\right|_0 \Delta T = \gamma T.$$

As a simple consequence of linearity, carbon stock changes in two experiments, E1 and E2, would add up to the carbon stock change in a third simulation, E3, given that $\Delta \mathrm{CO}_2^{\mathrm{E3}} = \Delta \mathrm{CO}_2^{\mathrm{E1}} + \Delta \mathrm{CO}_2^{\mathrm{E2}}$ and $\Delta T^{\mathrm{E3}} = T^{\mathrm{E1}} + T^{\mathrm{E2}}$. In the case of the COU, BGC, and RAD scenarios, we have $\Delta \mathrm{CO}_2^{\mathrm{COU}} = \Delta \mathrm{CO}_2^{\mathrm{BGC}}$ and $\Delta \mathrm{CO}_2^{\mathrm{RAD}} = 0$ since these simulations use prescribed atmospheric carbon dioxide concentrations. Further, we will demonstrate below (see section 4b) that the condition $\Delta T^{\mathrm{COU}} = \Delta T^{\mathrm{BGC}} + \Delta T^{\mathrm{RAD}}$ also holds for the simulations considered here. Consequently, for linear carbon cycle feedbacks, we would find

$$\Delta C^{\mathrm{COU}} = \Delta C^{\mathrm{BGC}} + \Delta C^{\mathrm{RAD}}. \tag{3}$$

We note the possibility that the basic assumption of carbon stocks being exclusively dependent on atmospheric CO_2 and T may be inadequate, and this assumption might be better replaced by $C = F(\mathrm{CO}_2, T, X)$ with an additional climate variable X. As long as it is possible to express X as a function of CO_2 or T, that is, $X = X(\mathrm{CO}_2, T)$, the general form of the feedback in (1) remains unchanged, while only the expression for the feedback parameters β and γ is modified (see Boer and Arora 2009). As an example, we mention export production, which, although not directly dependent on T, shows a clear relationship between SST and export changes (Schneider et al. 2008). The most obvious shortcoming of (1) and (2) is that no time dependence of inventory changes is included. In fact, it has been shown by Gregory et al. (2009) that considerably more carbon is taken up by land and ocean for slower rates of CO_2 increase. For this study, we only have one set of simulations using a rate of 1% yr^{-1} CO_2 increase available; therefore, we analyze the nonlinearity of carbon cycle feedbacks for this given rate of increase only.

3. Experiment description and analysis methods

We analyze the CMIP5 simulations with prescribed 1% yr^{-1} increase in atmospheric CO_2 (fully coupled simulation COU) together with the two related simulations BGC (biogeochemically coupled: only biogeochemistry code sees rising CO_2) and RAD (radiatively coupled: only radiation code sees rising CO_2). The preindustrial control simulation (CTR) is used to calculate changes relative to the control climate. At the time of writing, results from seven earth system models that have performed all four experiments were available in the CMIP5 database (Table 1).

Although the CO_2 concentration is fixed to the preindustrial value in the radiation code of the model in experiment BGC, it is known that near-surface air temperature usually increases somewhat in BGC-type model runs (e.g., Gregory et al. 2009; Boer and Arora 2009). This temperature increase is primarily caused by the physiological coupling of plant CO_2 uptake and evapotranspiration. An increasing stomatal closure under high CO_2 affects the balance of latent and sensible heat fluxes from plant canopies and thereby (among other effects) reduces the formation of low-level clouds (Sellers et al. 1996; Doutriaux-Boucher et al. 2009; de Arellano et al. 2012). Moreover, vegetation cover changes and increasing leaf area due to CO_2 fertilization can lead to surface albedo modifications and changes in dust mobilization (Zickfeld et al. 2011; Andrews et al. 2012). All of these processes change the radiative balance within the atmosphere and establish a radiative forcing that leads to surface warming (Doutriaux-Boucher et al. 2009). We call the warming due to this mechanism "CO_2 indirect warming" in the following text. Owing to the absence of CO_2 indirect warming in the RAD experiment, the surface climate in these simulations is slightly cooler than in the COU simulations, even though the same CO_2 forcing is applied in the models' radiation schemes. We investigate the impact of the CO_2 indirect warming on the CMIP5 simulations in section 4b. In all experiments the forcing due to non-CO_2 greenhouse gases and aerosols has been kept at preindustrial level and land-use change has been omitted.

The biogeochemically, radiatively and fully coupled simulations can be used in three combinations (COU–BGC, COU–RAD, and BGC–RAD) to estimate the carbon–concentration and carbon–climate feedbacks.

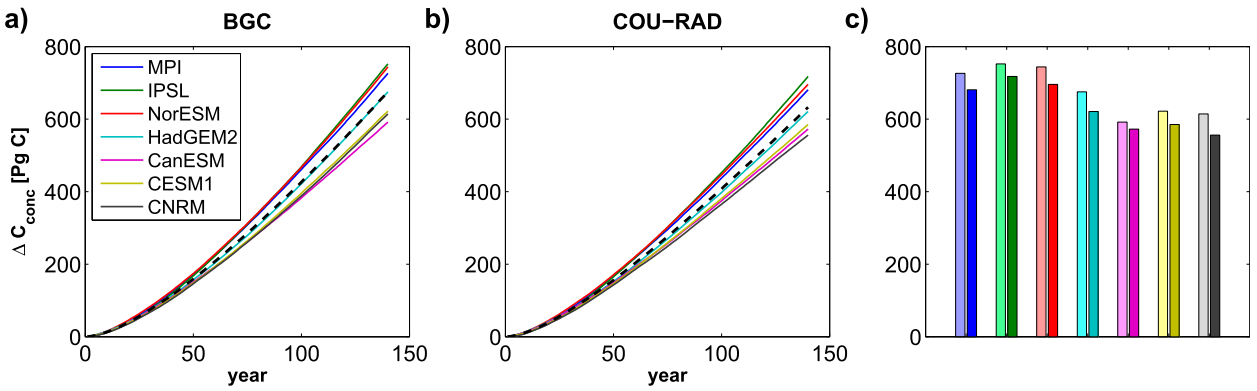

FIG. 1. Ocean carbon uptake (time-integrated air–sea carbon flux) due to the carbon–concentration feedback as derived from (a) the BGC simulation and (b) the difference in carbon uptake between the COU and RAD experiments. The model mean is given by the black dashed line. (c) The accumulated changes in ocean carbon stocks at the end of the simulations for both estimates, with the left (right) bar in each pair of bars representing the BGC (COU−RAD)-derived estimate. The color code for the seven models is given in (a).

This is exemplified in appendix A, where we derive three pairs of β and γ factors for the respective combinations of runs (e.g., $\beta^{\mathrm{COU–BGC}}$ and $\gamma^{\mathrm{COU–BGC}}$ are the feedback factors derived from the COU and BGC experiments). It turns out that the COU–RAD and BGC–RAD combinations result in the same estimate for the carbon–climate feedback (the corresponding feedback factor is denoted γ^{RAD} in the following text). Likewise, the COU–BGC and BGC–RAD combinations give a very similar carbon–concentration feedback estimate if ΔT^{BGC} is small [see (A3a) and (A3c) in appendix A]. Hence, only two distinct pairs of estimates for the carbon cycle feedbacks can be derived from the three simulations. In terms of carbon stock changes, the estimates for the carbon–climate feedback read $\Delta C^{\mathrm{COU}} - \Delta C^{\mathrm{BGC}}$ and ΔC^{RAD} and the respective γ factors can be obtained by dividing these carbon stock changes by the appropriate temperature increments [$\gamma^{\mathrm{COU–BGC}}$ and γ^{RAD}, see (A3d) and (A3e)].

For the carbon–concentration feedback, the situation is slightly more complex because ΔC^{BGC} generally includes temperature contributions due to CO_2 indirect warming ($\Delta T^{\mathrm{BGC}} \neq 0$), and because the CO_2 indirect forcing effect is absent in the RAD experiment ($\Delta T^{\mathrm{RAD}} < \Delta T^{\mathrm{COU}}$). Since, as discussed in section 4b, these temperature differences are relatively small, we adopt the somewhat simplified wording that ΔC^{BGC} and $\Delta C^{\mathrm{COU}} - \Delta C^{\mathrm{RAD}}$ represent estimates of changes in carbon stocks due to the carbon–concentration feedback [which would be strictly true in the case $\Delta T^{\mathrm{BGC}} = 0$ and $\Delta T^{\mathrm{RAD}} = \Delta T^{\mathrm{COU}}$, cf. (A3a) for $\beta^{\mathrm{COU–BGC}}$ and (A3b) for $\beta^{\mathrm{COU–RAD}}$].

We define ΔC^{nl}, the nonlinear part of the carbon inventory change, as the difference between the carbon uptake in the fully coupled experiment and the sum of the carbon uptake found in the biogeochemically and radiatively coupled experiments; that is,

$$\Delta C^{\mathrm{nl}} = \Delta C^{\mathrm{COU}} - (\Delta C^{\mathrm{BGC}} + \Delta C^{\mathrm{RAD}}), \qquad (4)$$

and similarly for other variables. Here ΔC^{nl} can be derived from the two estimates of the carbon–climate as well as the two estimates of the carbon–concentration feedback since $(\Delta C^{\mathrm{COU}} - \Delta C^{\mathrm{BGC}}) - \Delta C^{\mathrm{RAD}} = (\Delta C^{\mathrm{COU}} - \Delta C^{\mathrm{RAD}}) - \Delta C^{\mathrm{BGC}}$. Therefore, we focus the following analysis mostly on the nonlinearity of the carbon–climate feedback, keeping in mind that the nonlinearity of the carbon–concentration feedback as defined above is the same.

4. Results and discussion

a. *Carbon fluxes*

The cumulative ocean carbon uptake (calculated from modeled air–sea CO_2 fluxes) due to the carbon–concentration feedback as estimated by the BGC experiment ΔC^{BGC} and as calculated by the difference $\Delta C^{\mathrm{COU}} - \Delta C^{\mathrm{RAD}}$ is shown in Fig. 1 along with the change in ocean carbon inventory at the end of the 140-yr simulation period for the two cases. The carbon stock is consistently larger for all models at the end of the BGC simulation (compared to COU–RAD) by a range of 19 (CanESM2) to 58 (CNRM-CM5.2) Pg C. Hence, the BGC and the RAD simulation do not add up linearly to the carbon stock change of the COU experiment, that is, $\Delta C^{\mathrm{COU}} \neq \Delta C^{\mathrm{BGC}} + \Delta C^{\mathrm{RAD}}$), and we find a nonlinear contribution ΔC^{nl} of −19 to −58 Pg C in the CMIP5 models. Compared to the total carbon uptake ΔC^{COU}, which ranges from 533 to 676 Pg C, this nonlinearity is relatively small ($\Delta C^{\mathrm{BGC}} + \Delta C^{\mathrm{RAD}}$ is larger than ΔC^{COU} by 3.6%–10.6%).

A summary of the carbon–climate feedback derived from $\Delta C^{\mathrm{COU}} - \Delta C^{\mathrm{BGC}}$ and ΔC^{RAD} is given in Fig. 2.

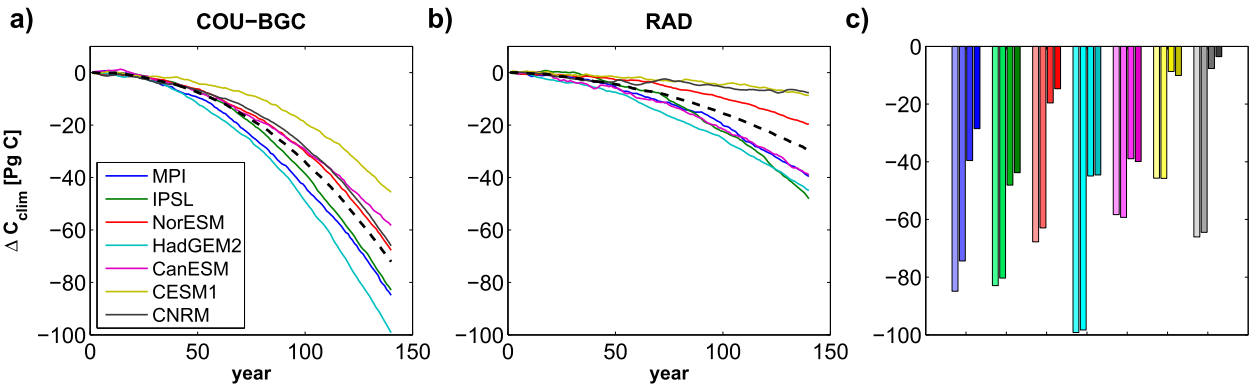

FIG. 2. Carbon release (time-integrated air–sea carbon flux) from the ocean due to the carbon–climate feedback as derived from (a) the difference in carbon uptake between the COU and BGC experiments and (b) the carbon release in the RAD simulation. The model mean is given by the black dashed line. (c) The changes in ocean carbon stocks at the end of the simulation period for both estimates, with the first (third) bar in each group of bars representing the COU–BGC (RAD)-derived estimate of total carbon: that is, the time-integrated air–sea carbon flux. The second (fourth) bar in each group of bars represents the changes in the total DIC inventory in the COU–BGC (RAD) experiments. The color code for the seven models is displayed in (a).

A reduction of the oceanic carbon stocks due to the impact of climate change is observed in both cases for all participating models: that is, ΔC_{clim} is negative across all models, regardless of which of the two estimates is used. While ΔC^{rad} ranges from −7.7 to −48 Pg C, the carbon–climate effect estimated by $\Delta C^{\text{COU}} - \Delta C^{\text{BGC}}$ is −46 to −99 Pg C. As mentioned above, ΔC^{nl}—that is, the −19 to −58 Pg C discrepancy between the two estimates of ΔC_{clim}—is the same as for the two estimates of ΔC_{CO2} by definition. However, owing to the much smaller overall ocean carbon–climate feedback, this discrepancy results in ΔC_{clim} estimates, which are up to a factor of 6 apart.

A summary of these results in terms of β and γ factors is given in Table 2. If the COU–BGC experiment pair is used to estimate the carbon cycle feedbacks (as in Friedlingstein et al. 2006), the model mean $\beta^{\text{COU–BGC}}$ and $\gamma^{\text{COU–BGC}}$ are 0.8 Pg C ppm^{-1} and −16.6 Pg C K^{-1}, respectively, while the corresponding COU–RAD-derived mean $\beta^{\text{COU–RAD}}$ and γ^{RAD} values are 0.75 Pg C ppm^{-1} and −6.7 Pg C K^{-1}.

We note that Arora et al. (2013) use the BGC and RAD experiments to quantify the carbon cycle feedbacks. In this approach, the γ factor is identical to γ^{RAD} while $\beta^{\text{BGC–RAD}} \approx \beta^{\text{COU–BGC}}$ for $\Delta T^{\text{BGC}} \approx 0$ (see appendix A). For the set of models considered here the difference between $\beta^{\text{BGC–RAD}}$ and $\beta^{\text{COU–BGC}}$ as given in Table 2 is small (<0.014). Arora et al. mention that, although feedback parameters are generally dependent on the scenario used, the ocean carbon–climate feedback derived from the CMIP5 model ensemble is weaker compared to the C^{4}MIP results (the mean $\gamma^{\text{COU–BGC}}$ value for the C^{4}MIP models is −30.9 Pg C K^{-1}). One factor explaining this discrepancy is the use of emission-driven scenarios in C^{4}MIP as opposed to concentration-driven scenarios in Arora et al. (2013), since the former lead to an overestimation of the magnitude of γ (Gregory et al. 2009; Zickfeld et al. 2011). A second factor explaining a substantial part of these differences is the approach chosen to calculate the feedback parameters, as indicated by our results above.

TABLE 2. Values of β (Pg C ppm^{-1}) and γ (Pg C K^{-1}) factors derived from the COU–BGC, COU–RAD, and BGC–RAD pairs of experiments. Note that $\gamma^{\text{COU–RAD}} = \gamma^{\text{BGC–RAD}} = \gamma^{\text{RAD}}$ (see appendix A).

Model	$\beta^{\text{COU–BGC}}$	$\beta^{\text{COU–RAD}}$	$\beta^{\text{BGC–RAD}}$	$\gamma^{\text{COU–BGC}}$	γ^{RAD}
MPI-ESM-LR	0.862	0.803	0.858	−19.0	−8.7
IPSL-CM5A-LR	0.898	0.850	0.892	−18.0	−10.2
NorESM1-ME	0.878	0.822	0.876	−18.1	−5.9
HadGEM2-ES	0.816	0.741	0.802	−21.9	−10.3
CanESM2	0.695	0.674	0.695	−11.2	−7.8
CESM1(BGC)	0.734	0.689	0.732	−11.9	−2.3
CNRM-CM5.2	0.722	0.654	0.722	−15.9	−1.9
Model mean	0.801	0.748	0.797	−16.6	−6.7

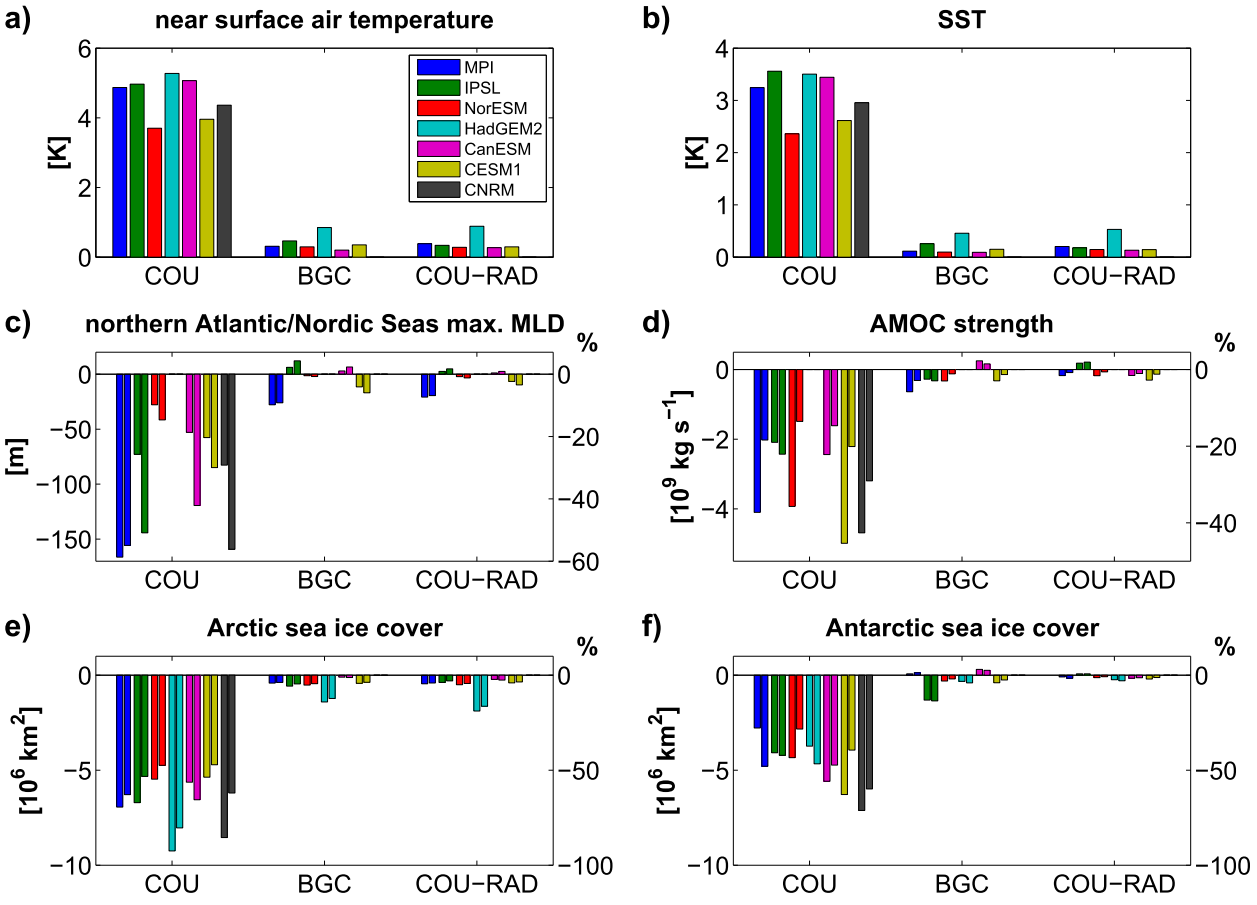

FIG. 3. Response (change relative to control simulation) of (a) global average near-surface air temperature, (b) global average sea surface temperature, (c) northern Atlantic/Nordic seas (defined here as the region 47°–80°N, 60°W–20°E) mean monthly maximum mixed layer depth, (d) Atlantic meridional overturning circulation strength (northward mass transport across 40°N), (e) Arctic sea ice cover, and (f) Antarctic sea ice cover. Values are displayed for the fully coupled simulation COU (left group of bars), for the BGC simulation (middle group of bars), and for the difference between the COU and RAD simulations (right group of bars). All values are mean values over the last 10 yr of the simulation period, except for (d) where the average over the whole simulation is given. In (c)–(f) the left part of each individual bar gives absolute values (left axis) while the right part of each bar shows fractional changes relative to the control simulation (right axis). The color code for the seven models is indicated in (a).

b. Summary of physical climate change in the different experiments

As a starting point for further analysis, we examine whether the nonlinearity of carbon cycle feedbacks described above could be caused by nonlinearities in physical climate in the different runs. That is, we investigate to what extent climate change due to CO_2 indirect warming is affecting the experiment BGC and, likewise, to what extent changes in the physical climate system differ in the COU and RAD experiments.

In the BGC simulations, most models show a near-surface air temperature increase of roughly 0.2–0.46 K toward the end of the 140-yr simulation period (Fig. 3a, numbers are mean values over the last 10 years of the simulations). The HadGEM2-ES responds considerably stronger with an increase of 0.85 K. We note that CNRM-CM5.2 does not employ a fully coupled land carbon cycle. Hence, there is no reaction of the plant canopy to elevated CO_2 levels and, consequently, for this model $\Delta T^{\mathrm{BGC}} = 0$. Compared to the temperature response (difference with the control experiment) of 3.7–5.3 K in the fully coupled simulation (Fig. 3a), the response in the BGC experiments remains below 10% of these values, except for HadGEM2-ES, where it is found to be 16%. A very similar picture emerges when evaluating $\Delta T^{\mathrm{COU}} - \Delta T^{\mathrm{RAD}}$, and we find a maximum difference of 0.13 K between ΔT^{COU} and $\Delta T^{\mathrm{BGC}} + \Delta T^{\mathrm{RAD}}$. Using a γ value of 20 Pg C K^{-1}, which is at the upper end of values calculated for the set of CMIP5 models (Table 2), this temperature nonlinearity translates into roughly 2.6 Pg C uptake nonlinearity. Since this value is small in

relation to the nonlinearity of 19–58 Pg C, we conclude that, for the purpose of this study, $\Delta T^{COU} \approx \Delta T^{BGC} + \Delta T^{RAD}$.

We further investigate whether changes in key variables for ocean carbon uptake are consistent with the surface air temperature responses found in the COU, BGC, and RAD simulations. That is, we check whether the use of temperature as a proxy for climate change could possibly be inadequate and thus (partly) responsible for the observed nonlinear carbon cycle feedbacks. For example, it would be inconsistent with the use of ΔT as a proxy for climate change if we would find a significant increase in, for example, ocean circulation strength in the BGC simulation, despite the fact that $\Delta T^{BGC} > 0$. Likewise, it would be inconsistent if circulation changes would be very different in the BGC experiment compared to changes in the COU relative to the RAD simulation (since $\Delta T^{BGC} \approx \Delta T^{COU} - \Delta T^{RAD}$).

Global mean sea surface temperature (SST, Fig. 3b) plays an important role for ocean carbon uptake since the Revelle factor (or buffer factor) of seawater (Revelle and Suess 1957; Zeebe and Wolf-Gladrow 2001) decreases with increasing temperature. SST also influences carbon uptake indirectly by impacting ocean circulation and stratification. The SST response in all experiments closely resembles (but is smaller than) the near-surface air temperature response, with values of 2.4–3.6 K in the fully coupled simulation. SST changes occurring in the BGC runs remain below 8% of these values, again with the exception of HadGEM2-ES, where the BGC SST response is 13% of the response in the COU experiment. Likewise, the nonlinearity (difference between ΔSST^{COU} and $\Delta SST^{BGC} + \Delta SST^{RAD}$; maximum value of 0.09 K) is consistent with the surface air temperature nonlinearity. We note that the SST nonlinearity can reach values up to 2 K (mean over the last 10 years of the experiments) regionally. These relatively large regional discrepancies are caused by modes of interannual- to decadal-scale variability, which evolve slightly differently in BGC compared to COU–RAD (not shown). Since the SST responses over the 140 years are smaller than the amplitude of variability, we conclude that they are not significantly different for the purpose of this study.

The northern Atlantic and Nordic seas (defined here as the region between 47° and 80°N, 60°W and 20°E) are the world's most intense carbon uptake regions per unit area (Takahashi et al. 2009). This uptake is sustained by carbon transport to depth through deep-water formation and subsequent southward transport by the Atlantic meridional overturning circulation (AMOC). Therefore, changes in northern Atlantic/Nordic seas maximum mixed layer depth (MMLD, Fig. 3c) and in AMOC strength (Fig. 3d) are expected to influence carbon uptake and sequestration. MMLD as well as AMOC strength decrease clearly in the fully coupled simulations for all models, and both quantities show considerably weaker trends in the BGC simulation as well as in the difference between the COU and RAD experiments. Small inconsistencies with the temperature response can be observed for some models. For example, MMLD slightly increases for IPSL-CM5A-LR and CanESM2 in the BGC experiment as well as in COU–RAD, despite a global temperature increase. Likewise, MMLD and AMOC strength reduction in MPI-ESM-LR is larger in BGC than in COU–RAD, although the global near-surface temperature increase is slightly smaller in the BGC experiment. As for SST, the responses of MMLD and AMOC in the BGC experiment and in the COU relative to the RAD simulation are dominated by interannual- to decadal-scale variability (i.e., the response over the 140 years is smaller than the amplitude of variability), and hence the small inconsistencies found here do not indicate significant differences between the two cases.

The sea ice area response in the COU and BGC simulations as well as the difference COU–RAD for Arctic and Antarctic are shown in Figs. 3e,f. The Arctic sea ice cover in the BGC simulations shows a small decline in all models, which is very similar to the ice cover differences seen in the COU relative to the RAD experiment. This Arctic sea ice decline is strongly correlated with the corresponding global surface air temperature and global SST increases. In the Southern Hemisphere, the modeled sea ice cover remains less affected by the CO_2 indirect warming in all models, except IPSL-CM5A-LR, which shows a noticeable Antarctic sea ice decline in the BGC simulation. The nonlinearity in sea ice cover is smaller than 0.5×10^6 km^2 for both Arctic and Antarctic with the exception of IPSL-CM5A-LR, which shows an Antarctic sea ice cover nonlinearity of 1.4×10^6 km^2. Assuming an accumulated carbon flux of 3 kg C m^{-2}, which is a typical value found for the Southern Ocean in the fully coupled simulations, we estimate, as an upper limit, that the ice area nonlinearity could contribute about 1.5 Pg C (4.2 Pg C for IPSL-CM5A-LR) to the simulated nonlinearity of carbon fluxes. The role of sea ice retreat is further investigated in the next section.

It is a limitation of this study that we cannot strictly disentangle the contribution of nonlinearities in climate to the simulated carbon flux nonlinearity. Additional model experiments (e.g., with CO_2 indirect warming switched off) would be required to quantify the role of various climatic factors. The results presented in this section do, however, not support the notion that climatic

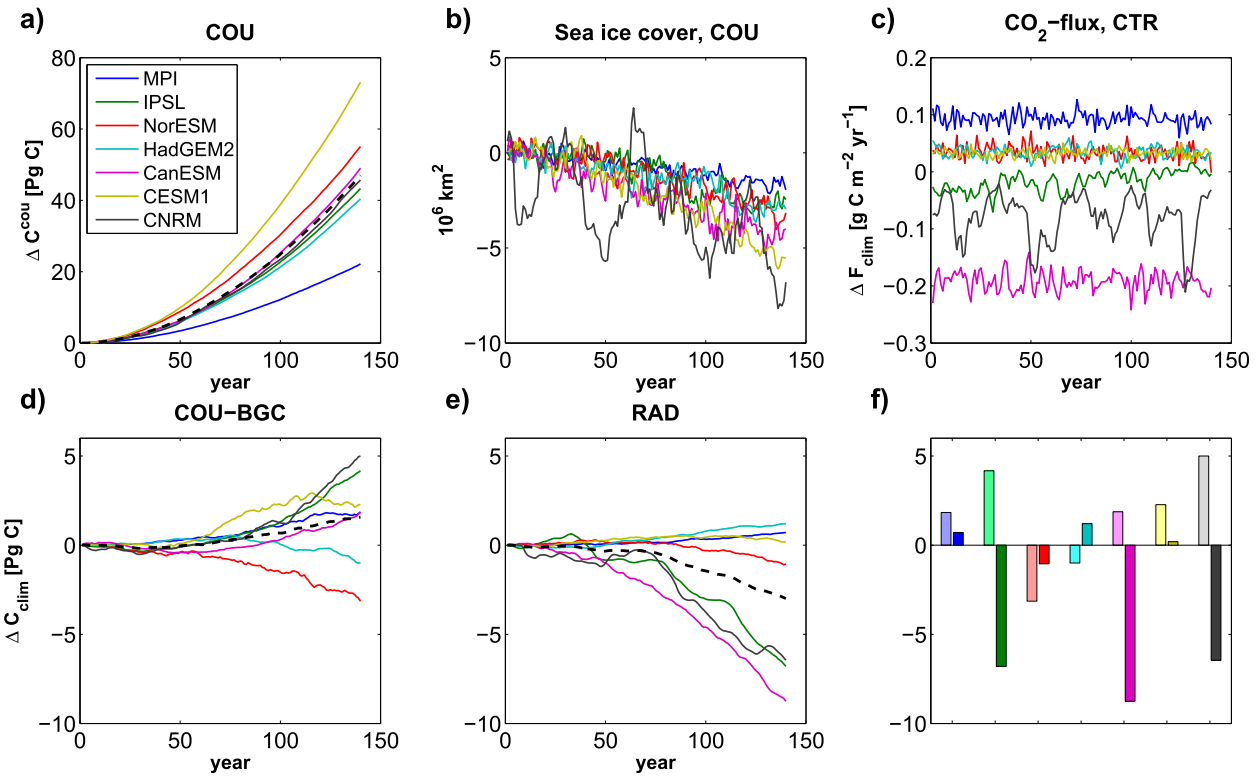

FIG. 4. Feedback analysis for Southern Hemisphere grid points that have a mean sea ice cover >30% in the control simulation: (a) cumulative carbon uptake and (b) changes in sea ice cover for the fully coupled simulation, (c) carbon fluxes for the control simulation (positive into the ocean), (d) difference in cumulative carbon uptake between the COU and BGC experiments, (e) cumulative carbon uptake in the RAD relative to the control simulation, and (f) changes in integrated air–sea carbon flux for both estimates at the end of the simulation period, with the left (right) bar in each pair of bars representing the COU–BGC (RAD)-derived estimates. The color code is indicated in (a).

differences between BGC and COU–RAD have a significant impact. We note that the CNRM-CM5.2, which does not include the CO_2 indirect warming effect, shows a carbon flux nonlinearity very similar to the other models. Nevertheless, this limitation adds some additional uncertainty to the results presented in this study.

c. *Nonlinearity due to sea ice*

Sea ice retreat under warming climate can potentially cause nonlinear carbon feedbacks, depending on whether climate warms under rising or preindustrial CO_2 levels. The mechanism behind this nonlinearity found by Zickfeld et al. (2011) in the Southern Ocean in their model is as follows. In the RAD simulation, carbon-rich upwelled waters release more CO_2 to the atmosphere as sea ice retreats with warming climate (positive carbon–climate feedback). In contrast, in the high CO_2 experiments COU and BGC, the rising atmospheric CO_2 partial pressure turns the outgassing into uptake, such that retreating sea ice leads to increased uptake in the fully coupled relative to the BGC experiment (negative carbon–climate feedback). Consequently, this kind of nonlinearity is expected only if there is a potential for carbon outgassing under the retreating ice cover.

To assess this mechanism for our CMIP5 model ensemble, we calculate accumulated carbon fluxes in grid cells that are ice covered in the control simulation. We define "ice-covered grid cell" as grid cells that have an average ice cover larger than 30% in the control simulation. In the Southern Hemisphere, the accumulated carbon uptake through these grid cells in the fully coupled simulations amounts to roughly 20–70 Pg C and the ice cover decreases by 2–6 $\times$ 10^6 km^2 (Figs. 4a,b). Figure 4c shows that three of the models considered here (IPSL-CM5A-LR, CanESM2, and CNRM-CM5.2) show an overall outgassing of CO_2 in this region in the control simulation. Likewise, these models show a considerable nonlinearity ΔC^{nl} of 10–12 Pg C, which is compatible with the mechanism described above (Figs. 4d,e; negative carbon climate feedback derived from

COU–BGC, positive feedback derived from the RAD experiment). For all other models we find a small nonlinearity of less than 2.2 Pg C (Fig. 4f), which is on the same order as the estimated nonlinearity due to differences in sea ice cover (section 4b). We note that the nonlinearity in Antarctic sea ice cover found for IPSL-CM5A-LR, acts to decrease the local nonlinearity in carbon uptake since the relatively large decrease in Antarctic sea ice in the BGC simulation increases carbon uptake and thus decreases the COU–BGC estimate of the carbon–climate feedback.

In the Northern Hemisphere (not shown) all models take up carbon in the ice-covered region in the control simulation, and the carbon–climate feedback is negative (increased carbon uptake due to climate change) for all models and irrespective of the estimate used, such that the nonlinearity is negligible on a global scale (less than 3 Pg C with varying sign).

d. Ocean DIC content

Carbon dioxide entering the surface ocean dissolves and forms carbonic acid, which dissociates to form bicarbonate and carbonate ions (Zeebe and Wolf-Gladrow 2001); the sum of all these species is known as dissolved inorganic carbon (DIC). DIC is converted to organic carbon by biological processes, and part of this organic carbon is exported out of the surface ocean to be remineralized at depth. Although this biological pump process is crucial for the distribution of carbon in the interior ocean, the standing stock of organic carbon in the ocean is small compared to the inorganic carbon stock. We note that none of the models considered here implement a sensitivity of biological production to increasing carbon availability (e.g., a change in organic carbon to nutrients ratio in organic matter) as, for instance, in Oschlies et al. (2008) or Tagliabue et al. (2011) with implications for carbon uptake. Likewise, none of the models implement a sensitivity of calcification to decreasing seawater pH. Therefore, in the models used here, we do not expect large nonlinearities due to differences in organic carbon production and export rates between the BGC–CTR and COU–RAD experiment pairs.

Figure 2c shows the two different ΔC_{clim} estimates derived from air–sea CO_2 fluxes together with the corresponding changes in ocean DIC content. The difference between ΔC_{clim} and ΔDIC is relatively small for all models and, more importantly, the nonlinear behavior is almost exactly the same. We therefore conclude that, on a global scale, changes in the integrated air–sea CO_2 flux translate directly into changes in ocean DIC content. Specifically, we assume that, under the linear feedback framework, (3) linking the carbon inventory changes in the different experiments would be transferable to changes in DIC inventory. In other words, we assume that the condition $\Delta\text{DIC}^{\text{COU}} \neq \Delta\text{DIC}^{\text{BGC}} + \Delta\text{DIC}^{\text{RAD}}$ is an indicator for nonlinear carbon cycle feedbacks, and in analogy to (4) we define a measure of nonlinear DIC stock changes as $\Delta\text{DIC}^{\text{nl}} = \Delta\text{DIC}^{\text{COU}} - (\Delta\text{DIC}^{\text{BGC}} + \Delta\text{DIC}^{\text{RAD}})$.

Figure 5a shows global mean profiles of DIC concentration changes for the COU experiment relative to BGC, and for the RAD relative to the control simulation. Carbon is lost from the ocean owing to climate change above 1000-m depth in all models for both estimates. Below 2000-depth, however, the DIC concentration is increasing in the RAD simulations in all models, whereas climate change generally leads to a decrease in DIC when estimated by COU–BGC. Between 2000- and 3000-m depths $\text{DIC}^{\text{COU}} - \text{DIC}^{\text{BGC}}$ is negative for all models. The difference between the COU–BGC and RAD–CTR cases, shown in Fig. 5b, is positive ($\text{DIC}^{\text{COU}} - \text{DIC}^{\text{BGC}}$ is less negative than $\text{DIC}^{\text{RAD}} - \text{DIC}^{\text{CTR}}$) above 400-m depth and negative ($\text{DIC}^{\text{RAD}} - \text{DIC}^{\text{CTR}} > \text{DIC}^{\text{COU}} - \text{DIC}^{\text{BGC}}$) below approximately 750 m for all models. Hence, we find a consistently distinct nonlinearity in shallow and deep water masses. Based on this result, we divide the water column into two compartments for the following analysis, the ''upper ocean'' above 500-m depth and the ''deep ocean'' below 500-m depth. We note that, although this separation of upper and deep ocean is not based on physical reasoning, the upper ocean roughly represents water masses that are well ventilated for large parts of the World Ocean, except for parts of the northern and eastern Pacific where old water masses reach shallower depths above 500 m. In terms of carbon mass, the upper ocean accumulates more than half of the DIC taken up in the fully coupled simulation: that is, 316–395 Pg C compared to 176–342 Pg C taken up by the deep ocean (Fig. 6a).

Figures 6b,c show the climate change impact on the DIC inventory calculated as $\Delta\text{DIC}^{\text{COU}} - \Delta\text{DIC}^{\text{BGC}}$ and $\Delta\text{DIC}^{\text{RAD}}$. Consistent with the profiles of DIC concentration changes shown in Fig. 5, these estimates are qualitatively similar for the upper ocean with the loss of carbon due to climate change being larger by −7.5 to −16 Pg C for the RAD simulation. The increase in DIC concentration below 500 m seen in the RAD simulations translates into an increase of deep ocean DIC content for most models, ranging from 4.7 to 39 Pg C. Only the HadGEM2-ES shows a slight deep ocean DIC decrease (−1.7 Pg C) in response to climate change in the RAD simulation. In contrast, deep ocean DIC decreases by −20 to −63 Pg C in the COU experiment relative to the BGC simulations at the end of the 140-yr period. For

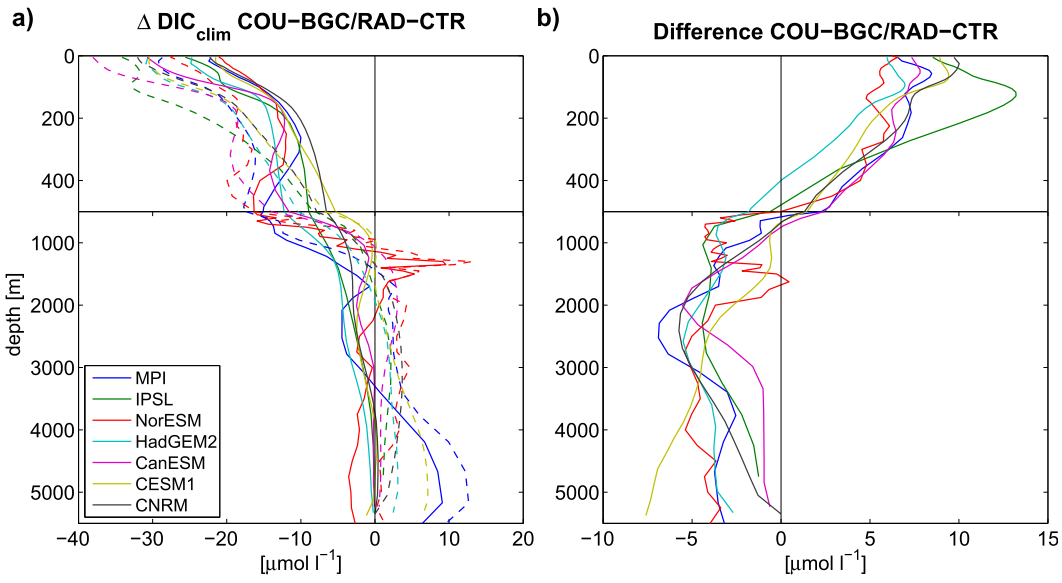

FIG. 5. Global mean profiles of (a) changes in ocean DIC concentration (mean value over the last 10 yr of the simulation period) derived from COU–BGC (solid lines) and RAD (dashed lines) and (b) the difference between the COU–BGC- and the RAD-derived estimate. The color code for the individual models is given in (a).

ΔDIC^{nl} we find values between 7.5 and 16 Pg for the upper ocean and between −33 Pg and −75 Pg for the deep ocean.

This finding is in line with the results of Zickfeld et al. (2011) and can be interpreted in terms of ocean circulation and stratification changes in the different experiments. In the COU and BGC simulations, where the ocean is taking up carbon, the carbon–climate feedback is determined by the amount of carbon that cannot be brought down to deeper depth because of increased ocean stratification (diagnosed with reduced mixing and reduced water mass transport in the North Atlantic, Fig. 3) in the COU experiment relative to BGC. In contrast, the RAD experiment shows a loss of carbon from the ocean. This loss, however, is mostly caused by depletion of upper-ocean DIC, while reduced overturning and mixing lead to increasing isolation of deep waters from the surface. Depending on the changes in circulation fields and associated changes in carbon pumps, these effects lead to almost constant or even increasing deep ocean DIC content. This reduced (or even reversed) climate change impact in the deep ocean seen in the RAD experiment is partly compensated by the surface ocean carbon–climate feedback. Here, the RAD experiment shows a stronger depletion of DIC in the upper 500 m compared to the corresponding reduction in DIC

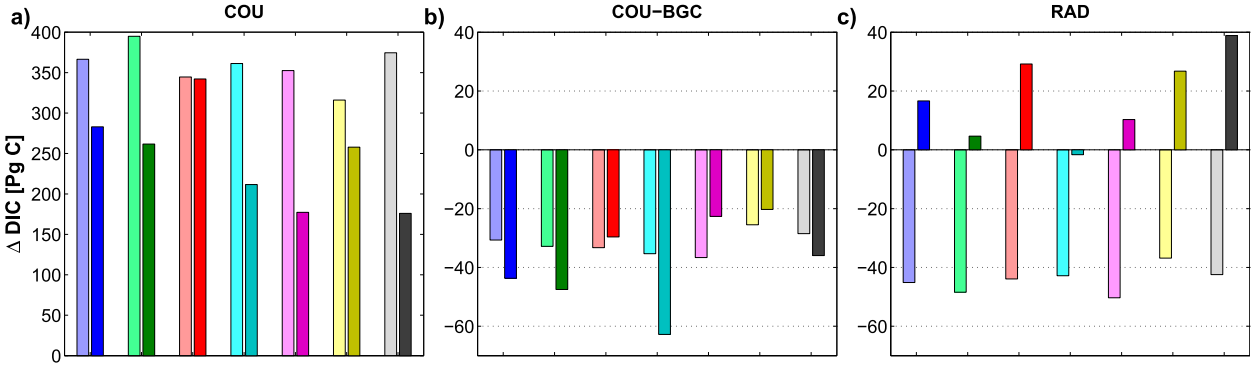

FIG. 6. Change in total DIC content over the 140-yr simulation period for (a) the COU, (b) the difference between COU and BGC, and (c) the RAD experiments. The two bars given for each model show the upper 500-m DIC content (left bar, lighter colors) and the deep ocean (below 500 m) DIC content (right bar, darker colors). The color code for the individual models is as in Fig. 5.

inventory found in the COU simulation relative to BGC. Both effects are investigated further in the following two subsections.

1) A LINEARIZED MODEL FOR UPPER-OCEAN DIC CONTENT

We assume that the upper-ocean carbon cycle feedback is dominated by the response of seawater carbon chemistry to climate change and rising CO_2 levels. To quantify the relative importance of different factors, we apply a simplified model for changes in surface ocean DIC concentration (using simulated annual mean fields of sea surface temperature, salinity, and alkalinity). We assume here that these surface changes are roughly representative for the upper ocean (0–500-m depth).

Since the partial pressure of CO_2 in seawater (pCO_2) is a function of temperature T, salinity S, DIC, and total alkalinity A, a variation in pCO_2 can be written using a first-order Taylor series approximation as

$$\delta pCO_2 = \frac{\partial pCO_2}{\partial T}\delta T + \frac{\partial pCO_2}{\partial S}\delta S + \frac{\partial pCO_2}{\partial \mathrm{DIC}}\delta \mathrm{DIC} + \frac{\partial pCO_2}{\partial A}\delta A .$$

Here, we are going to assume that the ocean under constant atmospheric CO_2 partial pressure acts to keep $\delta pCO_2 = 0$ from one year to the next. This assumption does not imply that there is no partial pressure difference, $\Delta pCO_2 = (pCO_2^{\mathrm{atm}} - pCO_2)$, across the air–sea interface. Rather, we assume that $\Delta pCO_2 =$ constant for annual mean values of two consecutive years. We further presume that pCO_2 variations due to biological activity and remineralization are, on an annual to interannual time scale, small enough to be neglected. In other words, for each change in pCO_2 caused by changing temperature, salinity, or alkalinity, a surface water parcel takes up or releases a corresponding amount of CO_2 in order to neutralize the pCO_2 change:

$$\delta \mathrm{DIC} \approx \left(\frac{\partial pCO_2}{\partial \mathrm{DIC}}\right)^{-1}\left[-\frac{\partial pCO_2}{\partial T}\delta T - \frac{\partial pCO_2}{\partial S}\delta S - \frac{\partial pCO_2}{\partial A}\delta A\right]. \quad (5)$$

If the atmospheric CO_2 partial pressure is not constant, there is an additional contribution to δDIC,

$$\delta \mathrm{DIC}^{\mathrm{atm}} = \frac{\partial \mathrm{DIC}}{\partial pCO_2^{\mathrm{atm}}}\delta pCO_2^{\mathrm{atm}},$$

which can be written in the same form as the individual terms of (5),

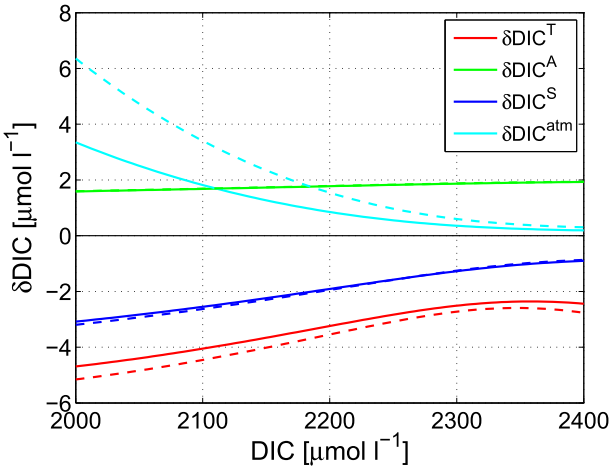

FIG. 7. Linear approximation of surface DIC change according to (5) and (6) for surface property variations $\delta T = +0.5$°C (red lines), $\delta S = +0.5$ psu (dark blue lines), $\delta A = +2\,\mu$mol l^{-1} (green lines), and $\delta pCO_2 = +4$ ppm (light blue lines) for a range of DIC values from 2000 to 2400 μmol l^{-1} and two different temperatures (5°C: dashed lines; 20°C: solid lines).

$$\delta \mathrm{DIC}^{\mathrm{atm}} \approx \left(\frac{\partial pCO_2}{\partial \mathrm{DIC}}\right)^{-1}\frac{\partial pCO_2}{\partial pCO_2^{\mathrm{atm}}}\delta pCO_2^{\mathrm{atm}}. \quad (6)$$

Since we assume $\Delta pCO_2 \approx$ constant, we have

$$\frac{\partial pCO_2}{\partial pCO_2^{\mathrm{atm}}} \approx 1.$$

We note that the term $\partial pCO_2/\partial$DIC is closely related to the Revelle factor, which is defined as

$$R = \frac{\mathrm{DIC}}{pCO_2}\frac{\partial pCO_2}{\partial \mathrm{DIC}}$$

(Revelle and Suess 1957; Zeebe and Wolf-Gladrow 2001).

For this study, we employ (5) and (6) to approximate variations in annual mean surface DIC due to modeled temperature, salinity, alkalinity, and atmospheric CO_2 changes ($\delta\mathrm{DIC}^T$, $\delta\mathrm{DIC}^S$, $\delta\mathrm{DIC}^A$, and $\delta\mathrm{DIC}^{\mathrm{atm}}$). Technical details and an evaluation of the method can be found in appendix B. Values of $\delta\mathrm{DIC}^T$, $\delta\mathrm{DIC}^S$, $\delta\mathrm{DIC}^A$, and $\delta\mathrm{DIC}^{\mathrm{atm}}$ calculated for a range of DIC concentrations (2000–2400 μmol l^{-1}) and at two different temperatures (5° and 20°C) using $\delta T = 0.5$°C, $\delta S = 0.5$ psu, $\delta A = 2\,\mu$mol l^{-1}, and $\delta pCO_2^{\mathrm{atm}} = 4$ ppm are given in Fig. 7. All resulting surface DIC variations become considerably smaller at high DIC except for $\delta\mathrm{DIC}^A$, which is slightly larger at high DIC values. This general behavior is found for both low and high temperatures.

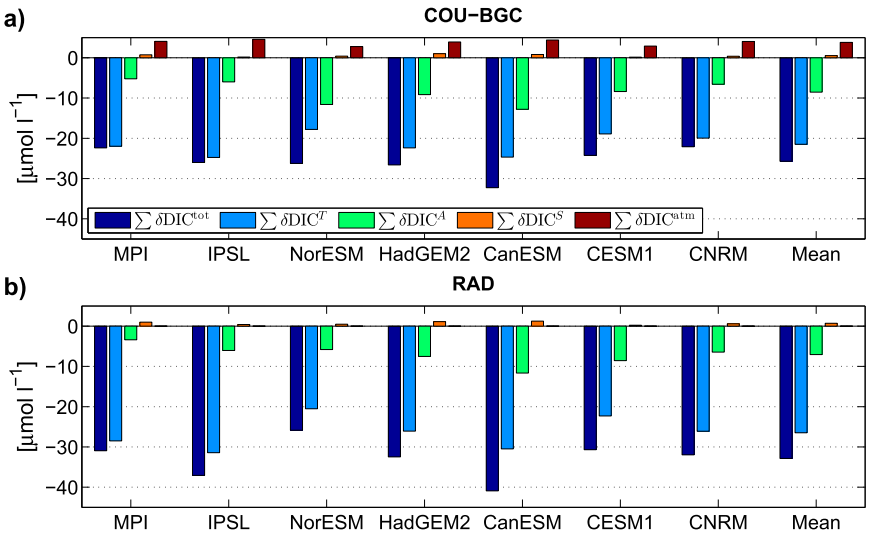

FIG. 8. Total decrease in surface DIC concentration due to climate change (dark blue) as modeled by the linearized surface ocean model (see text) and contributions of temperature (light blue), alkalinity (light green), salinity (orange), and atmospheric CO_2 variations (brown) to the total sum; shown are the estimates by (a) the difference between the COU and BGC simulations and (b) the RAD simulation.

The two estimates of the surface ocean carbon–climate feedback (COU–BGC and RAD) split into contributions from temperature, salinity, and alkalinity by means of the linear model are shown in Fig. 8. Changes in salinity and alkalinity mainly come from increased freshwater fluxes due to melting sea ice and enhanced runoff in the COU and RAD simulations. There is a small contribution of δDIC^{atm} to the COU–BGC estimate, which arises from slightly different Revelle factors in the two simulations. Although this result demonstrates that the carbon–concentration and carbon–climate feedbacks are coupled to some degree for the surface ocean, the magnitude of this effect is small. Increasing SST contributes most to the surface ocean carbon–climate feedback (55%–70% of the sum of all contributions in COU–BGC and 70%–86% in RAD) followed by alkalinity changes (16%–30% in COU–BGC and 10%–28% in RAD) while salinity changes are negligible on a global scale. Consistent with a larger sensitivity at low DIC concentrations (Fig. 7), SST change causes larger surface DIC decrease in the RAD simulation than in COU–BGC, while alkalinity variations cause larger carbon decline under high DIC. For most models, the nonlinearity due to SST increase is dominant. In NorESM, nonlinearities due to SST and alkalinity nearly cancel each other, leading to an almost equal surface DIC decrease in RAD as well as in COU–BGC (NorESM shows a relatively small SST response and relatively large alkalinity changes). In summary, the stronger surface ocean DIC decline in the RAD simulation compared to the COU–BGC estimate is primarily caused by the larger temperature sensitivity of the carbonate system at lower DIC concentration. The imprint of this behavior can be found down to approximately 500-m depth on a global scale (cf. Fig. 5b).

2) DEEP OCEAN DIC CONTENT

To better understand the strong nonlinearity in the deep ocean DIC, we compile a regional picture of this effect in terms of zonal means over different ocean basins in Fig. 9. The most significant nonlinearity ΔDIC^{nl} is found in the North Atlantic north of 20°N and in the waters south of 50°S. In both regions, $\Delta DIC^{COU}_{deep} - \Delta DIC^{BGC}_{deep}$ is clearly negative for all models: that is, less DIC is transported down into the deep ocean in the COU simulation compared to BGC. In contrast, ΔDIC^{RAD}_{deep} is generally near neutral or positive in both regions. The North Pacific shows a similar behavior for the RAD simulation: that is, a near-neutral or positive ΔDIC^{RAD}_{deep}. However, although $\Delta DIC^{COU}_{deep} - \Delta DIC^{BGC}_{deep}$ is found to be smaller than ΔDIC^{RAD}_{deep} for all individual models here, the large negative excursion of $\Delta DIC^{COU}_{deep} - \Delta DIC^{BGC}_{deep}$ found in the North Atlantic basin is absent in the northern Pacific region. In the tropics both estimates of the climate effect on deep ocean DIC are nearly equal: that is, there is little nonlinearity in a region extending from approximately 15°S to 15°N.

Upon examining cross sections of North Atlantic DIC in the different experiments (not shown), it becomes

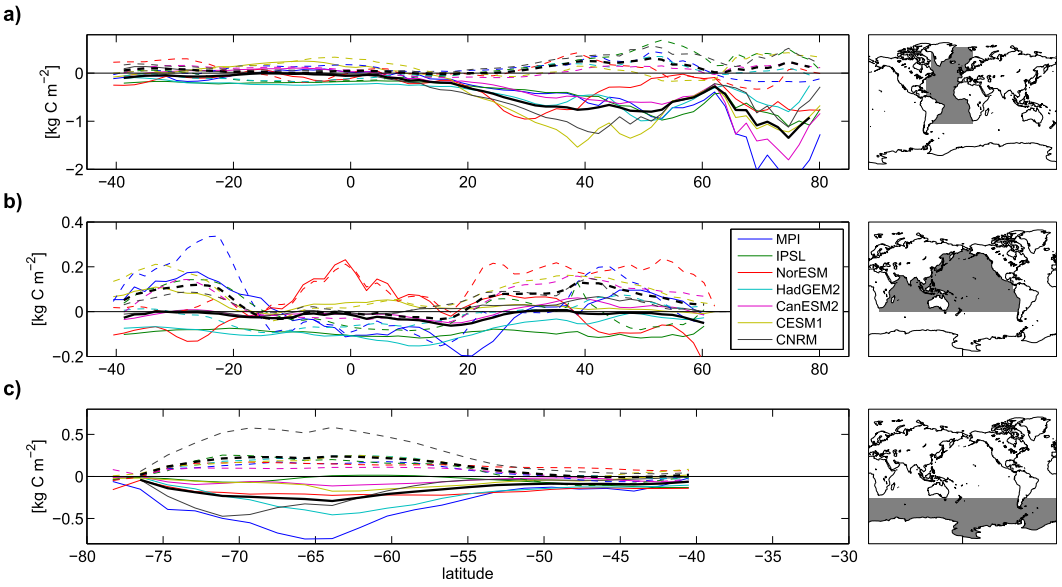

FIG. 9. Zonal means of deep ocean ΔDIC^{deep}_{clim} (column integral below 500-m depth; mean value over the last 10 yr of the simulation period) derived from COU–BGC (solid lines) and RAD (dashed lines) for (a) the Atlantic Ocean, (b) the Indian and Pacific Oceans, and (c) the waters south of 40°S. The color code for the individual models is given in (b), and mean values over all models are shown by thick black lines. The averaging region is indicated by the gray shaded domains in the right-hand panels.

apparent that the large climate effect on $\Delta DIC^{COU}_{deep} - \Delta DIC^{BGC}_{deep}$ is caused by the decrease of AMOC strength and deep water formation in the COU experiment, which has a strong effect on DIC invasion into the deep North Atlantic Ocean in all models. A similar weakening of the AMOC and reduction of mixed layer depth is present in the RAD simulation (cf. Fig. 3). However, since atmospheric CO_2 is not rising in this experiment, there is no surface to deep ocean flux, which is suppressed by reduced overturning and mixing. Rather, the deep ocean becomes more isolated from the surface leading to increasing DIC content (this issue is further discussed below). A similar picture emerges for the ocean south of 55°S. Here, too, we find $\Delta DIC^{RAD}_{deep} > 0$ and $\Delta DIC^{COU}_{deep} - \Delta DIC^{BGC}_{deep} < 0$ for all models with a maximum difference occurring between 60° and 70°S. We note that the largest portion of Southern Hemisphere anthropogenic carbon uptake and storage is characteristically found at lower latitudes north of 55°S, both in observation-based estimates (Sabine et al. 2004; Sallée et al. 2012) as well as in the CMIP5 models considered here (not shown). The deep ocean water masses south of 55°S mainly belong to Circumpolar Deep Water (CDW) and Antarctic Bottom Water (AABW), which are connected to the surface through the lower/southern branch of the Southern Ocean meridional overturning circulation (MOC) and through deep-water formation at the southern limb of the Southern Ocean (Sallée et al. 2013). While the upper/northern branch of the Southern Ocean MOC strengthens with increasing westerly wind intensity as climate warms, all CMIP5 models considered here simulate a weakening of the lower/southern branch (not shown). Hence, the deep ocean DIC nonlinearity appears to be consistently linked to a reduction of deep-water formation, in both the North Atlantic and Southern Ocean.

The increase of deep ocean DIC seen in the RAD experiment is accompanied by an increase in remineralization below 500-m depth. We demonstrate this by calculating the apparent oxygen utilization (AOU) for the different experiments. AOU indicates the total oxygen consumption by organic carbon remineralization since a water parcel left the surface: that is, the difference between the saturation concentration (Weiss 1970) and the in situ concentration. Figure 10 shows the differences in apparent oxygen utilization below 500 m for COU–BGC and RAD as zonal means. Positive AOU differences indicate that a water parcel has experienced more remineralization of organic carbon. Generally, the reduced overturning circulation in the COU and RAD experiments leads to higher AOU nearly everywhere because of longer water-mass residence times in the deep ocean. At the same time, the export production (export across 100-m depth) decreases globally in all models (not shown) by approximately 6%–20%, except in the region south of 40°S where it stays constant or

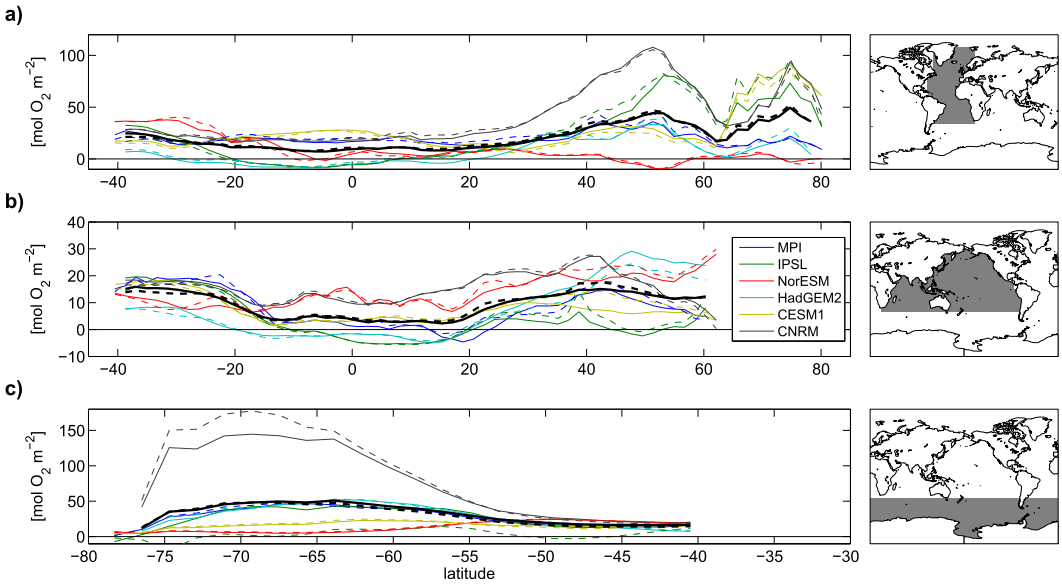

FIG. 10. As in Fig. 9, but for apparent oxygen utilization (AOU).

shows an increasing trend in some models. Hence, the higher AOU indicates that the generally decreased particle rain from the euphotic zone is overcompensated by a longer residence time of water masses in the deep ocean on a global scale. This result is consistent with the finding of Matear and Hirst (1999) that ocean CO_2 uptake in their model increases in response to circulation changes alone (i.e., when warming-induced outgassing is suppressed). Likewise, the increase in deep ocean AOU is consistent with the modeling study by Bernardello et al. (2013), who find that an increase of remineralized DIC outweighs reduced preformed DIC concentrations under changing climate. Interestingly, the climatic effect on AOU is virtually identical whether estimated by the RAD experiment or by COU–BGC (see Fig. 10; an exception to this statement is the IPSL-CM5A-LR in the Southern Ocean, where the AOU is elevated in the COU–BGC estimate while almost unchanged in the RAD simulation). This result indicates that generally very similar changes of particle rain versus deep ocean residence times also occur in the COU experiment relative to BGC. However, this effect is masked by the strong climate induced suppression of carbon drawdown into the deep ocean in the COU simulation.

5. Summary and conclusions

In this study, we quantify the nonlinearity of ocean carbon cycle feedbacks in CMIP5 earth system models for idealized experiments. If the feedback was linear, the carbon–concentration and carbon–climate feedbacks could be derived from two simulations: namely, a biogeochemically coupled simulation (BGC, "constant climate under rising CO_2") and a radiatively coupled simulation (RAD, "climate change under constant CO_2"). These two independent carbon cycle feedbacks would then add up to the carbon cycle feedback found in a fully coupled (COU) standard simulation. CMIP5 earth system models, however, consistently show that the ocean carbon cycle feedback is nonlinear. The magnitude of this nonlinearity, compared to the total ocean carbon feedback, is relatively small (3.6%–10.6%). However, in relation to the ocean carbon–climate feedback, which is the smaller contribution to the total feedback, the nonlinearity is of the same order of magnitude as the feedback itself. While the climate change under constant CO_2 type simulations (RAD) show from −7.7 to −48 Pg C release to the atmosphere, the climate feedback estimate derived by taking the difference between the COU and BGC simulations yields from −46 to −99 Pg C. The main reason for this discrepancy is that the carbon distribution and carbon gradients evolve very differently in the RAD simulation compared to the COU and BGC experiments: While in RAD the feedback is due to a loss of carbon mainly from the upper ocean, the feedback in the COU relative to the BGC simulation arises owing to a reduction of carbon transport to the deep ocean.

We find that the retreat of sea ice in regions that initially (i.e., in the control simulation) act as a source of CO_2 to the atmosphere may locally cause large nonlinear carbon cycle feedbacks. Three out of the seven CMIP5 models simulate a CO_2 source in the Antarctic sea ice region in the control experiment, and these

models consistently show a relatively large nonlinearity of 11 Pg C (1.9–5 Pg C uptake in COU relative to BGC but from −6.5 to −8.8 Pg C loss in RAD). The sign of this nonlinearity is opposite of what is simulated globally, and hence the sea ice mechanism tends to counteract the global feedback nonlinearity. The other models show only small nonlinearities (less than 2.2 Pg C with varying sign) in the Antarctic sea ice region. In the Arctic, none of the models simulate CO_2 outgassing under retreating sea ice. Consequently, the nonlinearity in carbon cycle feedbacks is small there (less than 3 Pg C with varying sign). We therefore conclude that sea ice retreat generally does not cause a globally significant nonlinearity of carbon cycle feedbacks in the models considered here.

In the upper 500 m of the water column, approximately, the sign of the carbon cycle nonlinearity is also found to be reversed compared to the total feedback nonlinearity. Here, the loss of carbon in the RAD simulations amounts to −37 to −50 Pg, while the COU–BGC estimate shows a reduction in carbon uptake of −26 to −37 Pg. A linearized carbon chemistry scheme has been employed to explore the contribution of seawater carbon chemistry to the surface ocean nonlinearity, assuming that this analysis is roughly representative for the upper ocean (0–500 m). Carbon uptake/release in response to SST and salinity (alkalinity) variations is larger (smaller) at low CO_2 concentrations. We find that SST changes contribute most to the surface carbon–climate feedback in the CMIP5 models (55%–70% of the sum of all contributions in COU–BGC and 70%–86% in RAD). Alkalinity plays the second largest role (16%–30% in COU–BGC and 10%–28% in RAD) while the role of salinity is negligible. In summary, we find that the reversed sign of the upper-ocean carbon cycle nonlinearity can be explained by the nonlinear chemistry of the carbonate system. That is, the upper-ocean carbon–climate feedback is larger rather than smaller in the RAD experiment owing to the higher sensitivity of the carbonate system to changes in temperature at lower DIC concentrations. Although more than 50% of carbon taken up by the ocean is found in the upper 500-m water column in the 1% CO_2 yr^{-1} scenario considered here, the upper-ocean carbon cycle nonlinearity is relatively small (7.5–16 Pg C).

The largest nonlinearity within the ocean carbon cycle feedback loop is simulated in the deep ocean dissolved inorganic carbon content (below 500 m). Increasing DIC inventories (4.7–39 Pg C) with proceeding climate change are found in the RAD experiments for all but one model (which shows a slight deep ocean DIC decrease of −1.7 Pg C). We find that this enhanced deep ocean carbon storage is caused by longer water-mass residence times overcompensating a generally reduced particle rain from the surface ocean. The same residence time versus particle rain changes, identified by a similar apparent oxygen utilization pattern, is simulated in the COU scenarios. However, the overall climate impact on the deep ocean carbon inventory under rising CO_2 levels (COU–BGC estimate) is a clear reduction of deep ocean DIC in all models (from −20 to −63 Pg C) since the dominant process in this feedback loop is the decreased downward transport of carbon owing to reduced circulation and mixing.

The key regions for ocean carbon cycle feedbacks are, consistent with previous studies, the North Atlantic and the Southern Ocean. At the same time, these regions exhibit the strongest nonlinearities as well as the largest intermodel spread in climate change impact on carbon uptake and storage. We find that in the Southern Hemisphere the nonlinearity is not tied to the main carbon uptake regions. Rather, the strongest nonlinearity in deep ocean carbon storage is found in the region south of 55°S where comparatively little anthropogenic carbon is taken up and stored. This nonlinearity appears to be associated with the southern and lower cell of the Southern Ocean water mass circulation. To reduce uncertainties in carbon cycle feedback projections, it is important to better understand and model the processes governing carbon uptake and storage in the North Atlantic and Southern Ocean.

The fully, radiatively, and biogeochemically coupled simulations can be used in three different combinations to quantify the carbon cycle feedbacks. Our results indicate that using the BGC–RAD combination is inconsistent with regard to total carbon uptake since the sum of the ocean carbon–concentration and carbon–climate feedbacks calculated this way is larger by 19–58 Pg C than the total feedback found in the fully coupled simulation. Using either experiment pair COU–BGC or COU–RAD is consistent but involves a different interpretation of the feedbacks. For example, the carbon–climate feedback calculated using the RAD experiment quantifies the impact of climate change on ocean carbon fluxes at constant CO_2 levels, while the difference between the COU and BGC simulations gives the climate change impact under rising CO_2. Since the latter would be the quantity of interest for most applications, we recommend using the COU–BGC pair of simulations for the quantification of ocean carbon cycle feedbacks in concentration-driven experiments.

Our results show that the perturbation of the ocean carbon cycle in the 1% scenario is too large to rely on a simple linear feedback analysis. Further, Gregory et al. (2009) demonstrated that the carbon–concentration feedback is strongly dependent on the rate of change of

atmospheric CO_2 and hence scenario dependent. In view of these results, future research should be directed toward finding an improved formalism for carbon cycle feedback quantification.

Acknowledgments. We thank three anonymous reviewers for their constructive and helpful comments on this paper. The research leading to these results was supported through the projects COMBINE and CARBOCHANGE, which received funding from the European Commission's Seventh Framework Programme under Grant Agreement 226520 and Grant Agreement 264879, respectively. JFT was supported by the Research Council of Norway funded project EarthClim (207711/E10). JS, JFT, and CH acknowledge the NOTUR projects nn2980k and nn2345k as well as the NorStore projects ns2980k and ns2345k for supercomputer time and storage resources. CDJ and IT were supported by the Joint DECC/Defra Met Office Hadley Centre Climate Programme (GA01101). We acknowledge the World Climate Research Programme's Working Group on Coupled Modelling, which is responsible for CMIP, and we thank the climate modeling groups (listed in Table 1 of this paper) for producing and making available their model output. For CMIP, the U.S. Department of Energy's Program for Climate Model Diagnosis and Intercomparison provides coordinating support and led development of software infrastructure in partnership with the Global Organization for Earth System Science Portals. This publication is a contribution to the Centre for Climate Dynamics within the Bjerknes Centre.

APPENDIX A

Carbon Cycle Feedback Metrics

As outlined by Arora et al. (2013, their appendix A1), the model simulations COU, BGC, and RAD can be used in three combinations to estimate the carbon–concentration and carbon–climate feedbacks. If feedbacks are linear, all three estimates would be identical. Let us consider two model experiments, E1 and E2, following different CO_2–T trajectories (through a full or partial decoupling of CO_2 and temperature change in at least one of the experiments):

$$\Delta C^{E1} = \beta \Delta CO_2^{E1} + \gamma T^{E1} \quad \text{and}$$
$$\Delta C^{E2} = \beta \Delta CO_2^{E2} + \gamma T^{E2}. \tag{A1}$$

The general solution of (A1) in terms of β and γ is given by

$$\beta = (\Delta C^{E1}\Delta T^{E2} - \Delta C^{E2}\Delta T^{E1})/d \quad \text{and}$$
$$\gamma = (\Delta C^{E2}\Delta CO_2^{E1} - \Delta C^{E1}\Delta CO_2^{E2})/d, \tag{A2}$$

where $d = \Delta CO_2^{E1}\Delta T^{E2} - \Delta CO_2^{E2}\Delta T^{E1}$. We can solve for β and γ using the COU–BGC, COU–RAD, or BGC–RAD experiment pairs, and the resulting three pairs of estimates for β and γ read

$$\beta^{COU-BGC} = \frac{\Delta C^{BGC}\Delta T^{COU} - \Delta C^{COU}\Delta T^{BGC}}{\Delta CO_2(\Delta T^{COU} - \Delta T^{BGC})} \approx \frac{\Delta C^{BGC}}{\Delta CO_2}, \tag{A3a}$$

$$\beta^{COU-RAD} = \frac{\Delta C^{RAD}\Delta T^{COU} - \Delta C^{COU}\Delta T^{RAD}}{\Delta CO_2\Delta T^{RAD}} \approx \frac{\Delta C^{COU} - \Delta C^{RAD}}{\Delta CO_2}, \tag{A3b}$$

$$\beta^{BGC-RAD} = \frac{\Delta C^{BGC}\Delta T^{RAD} - \Delta C^{RAD}\Delta T^{BGC}}{\Delta CO_2\Delta T^{RAD}} \approx \frac{\Delta C^{BGC}}{\Delta CO_2}, \tag{A3c}$$

$$\gamma^{COU-BGC} = \frac{\Delta C^{COU} - \Delta C^{BGC}}{\Delta T^{COU} - \Delta T^{BGC}} \approx \frac{\Delta C^{COU} - \Delta C^{BGC}}{\Delta T^{COU}}, \tag{A3d}$$

$$\gamma^{COU-RAD} = \frac{\Delta C^{RAD}}{\Delta T^{RAD}}, \quad \text{and} \tag{A3e}$$

$$\gamma^{BGC-RAD} = \frac{\Delta C^{RAD}}{\Delta T^{RAD}}. \tag{A3f}$$

The approximations given in (A3a)–(A3d) are applicable if $\Delta T^{BGC} \approx 0$ and/or $\Delta T^{COU} \approx \Delta T^{RAD}$. Since $\Delta CO_2^{RAD} = 0$, it turns out that the two estimates $\gamma^{COU-RAD}$ and $\gamma^{BGC-RAD}$ are identical (hence, we denote the γ factor derived from either the COU–RAD or BGC–RAD experiment pairs γ^{RAD}). Likewise, since $\Delta CO_2^{COU} = \Delta CO_2^{BGC}$ in the set of simulations used for this study, the β estimates derived from COU–BGC and BGC–RAD are equal in the limit of zero temperature change ΔT^{BGC}. We note that the experiment RAD was not carried out by the C^{4}MIP model ensemble; hence, Friedlingstein et al. (2006) used the COU–BGC estimates in their study, while Arora et al. (2013) chose the BGC–RAD approach.

APPENDIX B

Implementation of the Linear Surface DIC Model

The linearized surface ocean DIC scheme employed in section 4d(1) is implemented as follows. The seawater

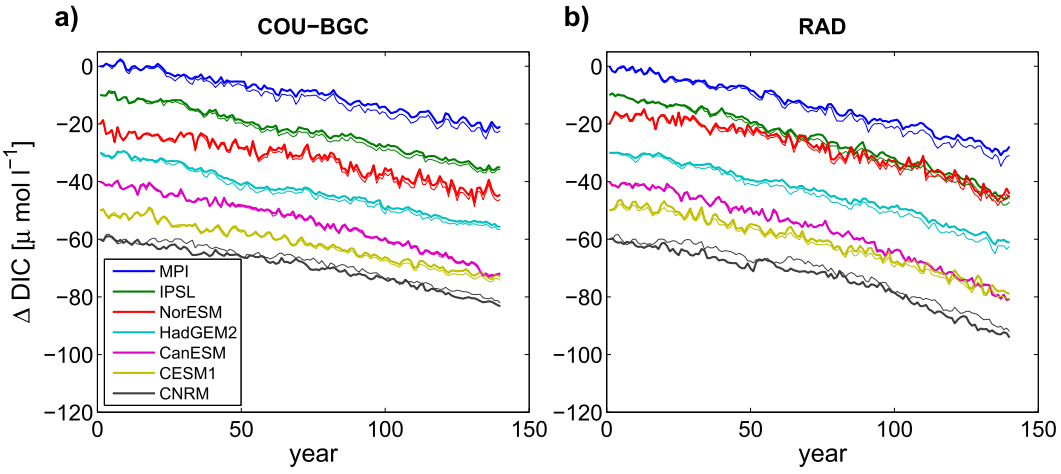

FIG. B1. Climate change impact on surface DIC concentration estimated by (a) the difference between the COU and BGC simulations and (b) the RAD simulation. Shown are the results calculated by the seven earth system models (thick lines) and as approximated by integrating the linear model described in section 4d(1) and appendix B based on changes in surface temperature, salinity, and alkalinity (thin lines). The results for each model are successively offset by $-10\,\mu\text{mol}\,\text{l}^{-1}$ to improve the readability of the graph.

carbonate system including the borate buffer is solved for $p\text{CO}_2$ as described in Zeebe and Wolf-Gladrow (2001) using annual mean surface fields (results of the participating CMIP5 models) of DIC, total alkalinity A, temperature T, and salinity S. The solubility of CO_2 in seawater (K_0) is calculated according to Weiss (1974), and the dissociation constants of CO_2 and boric acid (K_1, K_2, and K_b) and the ion product of water (K_w) are taken from Dickson and Millero (1987), Dickson (1990), and Millero (1995), respectively. Although the models generally include the contributions of minor bases like phosphate and silicate to total alkalinity, we neglect these contributions here. The derivatives of $p\text{CO}_2$ with respect to DIC, A, T, and S are calculated using a second-order difference scheme; for example,

$$\frac{\partial p\text{CO}_2(\text{DIC},A,T,S)}{\partial T} \approx \frac{p\text{CO}_2(\text{DIC},A,T+\Delta T,S)-p\text{CO}_2(\text{DIC},A,T-\Delta T,S)}{2\Delta T}$$

for a small temperature perturbation ΔT. We integrate the linear model by using differences in annual mean values between years i and $i-1$, for example, $\delta T_i = T_i - T_{i-1}$, where $i = 2, \ldots, 140$, to derive the corresponding contributions to δDIC. The calculations are performed grid point wise and global δDIC values are finally obtained by averaging over all model grid points. The results for surface DIC change relative to the simulation start year is then obtained by summing up all annual contributions, $\widehat{\Delta\text{DIC}} = \sum\delta\text{DIC}_i$. As demonstrated in Figs. B1a,b for the COU–BGC and RAD simulations, respectively, the linear model is able to reproduce both the interannual variability and the long-term trend very well. We note that for the simulations with rising CO_2 (COU and BGC) there is an overestimation of δDIC_i leading to $\widehat{\Delta\text{DIC}} > \Delta\text{DIC}$ by approximately 10% at the end of the 140-yr period (not shown). The reason for this overestimation is that the approximation $\Delta p\text{CO}_2 = (p\text{CO}_2^{\text{atm}} - p\text{CO}_2) \approx \text{constant}$ is violated to some extent for scenarios with rapid increase in atmospheric CO_2. Nevertheless, for the difference COU − BGC, the results from the linear model are similarly close to the full model results as for the RAD simulation (Fig. B1).

REFERENCES

Andrews, T., M. A. Ringer, M. Doutriaux-Boucher, M. J. Webb, and W. J. Collins, 2012: Sensitivity of an Earth system climate model to idealized radiative forcing. *Geophys. Res. Lett.,* **39,** L10702, doi:10.1029/2012GL051942.

Arora, V. K., and Coauthors, 2011: Carbon emission limits required to satisfy future representative concentration pathways of greenhouse gases. *Geophys. Res. Lett.,* **38,** L05805, doi:10.1029/2010GL046270.

——, and Coauthors, 2013: Carbon–concentration and carbon–climate feedbacks in CMIP5 Earth system models. *J. Climate,* **26,** 5289–5314, doi:10.1175/JCLI-D-12-00494.1.

Assmann, K. M., M. Bentsen, J. Segschneider, and C. Heinze, 2010: An isopycnic ocean carbon cycle model. *Geosci. Model Dev.,* **3,** 143–167, doi:10.5194/gmd-3-143-2010.

Aumont, O., and L. Bopp, 2006: Globalizing results from ocean in situ iron fertilization studies. *Global Biogeochem. Cycles,* **20,** GB2017, doi:10.1029/2005GB002591.

Bernardello, R., I. Marinov, J. B. Palter, J. L. Sarmiento, E. D. Galbraith, and R. D. Slater, 2013: Response of the ocean

natural carbon storage to projected twenty-first-century climate change. *J. Climate,* **27,** 2033–2053, doi:10.1175/JCLI-D-13-00343.1.

Boer, G. J., and V. Arora, 2009: Temperature and concentration feedbacks in the carbon cycle. *Geophys. Res. Lett.,* **36,** L02704, doi:10.1029/2008GL036220.

——, and ——, 2013: Feedbacks in emission-driven and concentration-driven global carbon budgets. *J. Climate,* **26,** 3326–3341, doi:10.1175/JCLI-D-12-00365.1.

Collins, W. J., and Coauthors, 2011: Development and evaluation of an Earth-system model—HadGEM2. *Geosci. Model Dev.,* **4,** 1051–1075, doi:10.5194/gmd-4-1051-2011.

Cox, P., R. Betts, C. Jones, S. Spall, and I. Totterdell, 2000: Acceleration of global warming due to carbon-cycle feedbacks in a coupled climate model. *Nature,* **408,** 184–187, doi:10.1038/35041539.

de Arellano, J. V.-G., C. C. van Heerwaarden, and J. Lelieveld, 2012: Modelled suppression of boundary-layer clouds by plants in a CO_2-rich atmosphere. *Nat. Geosci.,* **5,** 701–704, doi:10.1038/ngeo1554.

Dickson, A. G., 1990: Thermodynamics of the dissociation of boric acid in synthetic seawater from 273.15 to 318.15 K. *Deep-Sea Res. I,* **37,** 755–766, doi:10.1016/0198-0149(90)90004-F.

——, and F. J. Millero, 1987: A comparison of the equilibrium constants for the dissociation of carbonic acid in seawater media. *Deep-Sea Res. I,* **34,** 1733–1743, doi:10.1016/0198-0149(87)90021-5.

Doutriaux-Boucher, M., M. J. Webb, J. M. Gregory, and O. Boucher, 2009: Carbon dioxide induced stomatal closure increases radiative forcing via a rapid reduction in low cloud. *Geophys. Res. Lett.,* **36,** L02703, doi:10.1029/2008GL036273.

Dufresne, J.-L., L. Fairhead, H. Le Treut, M. Berthelot, L. Bopp, P. Ciais, P. Friedlingstein, and P. Monfray, 2002: On the magnitude of positive feedback between future climate change and the carbon cycle. *Geophys. Res. Lett.,* **29,** doi:10.1029/2001GL013777.

——, and Coauthors, 2013: Climate change projections using the IPSL-CM5 Earth system model: From CMIP3 to CMIP5. *Climate Dyn.,* **40,** 2123–2165, doi:10.1007/s00382-012-1636-1.

Eriksson, E., 1963: Possible fluctuations in atmospheric carbon dioxide due to changes in properties of sea. *J. Geophys. Res.,* **68,** 3871–3876, doi:10.1029/JZ068i013p03871.

Friedlingstein, P., J. Dufresne, P. Cox, and P. Rayner, 2003: How positive is the feedback between climate change and the carbon cycle? *Tellus,* **55B,** 692–700, doi:10.1034/j.1600-0889.2003.01461.x.

——, and Coauthors, 2006: Climate–carbon cycle feedback analysis: Results from the C^4MIP model intercomparison. *J. Climate,* **19,** 3337–3353, doi:10.1175/JCLI3800.1.

Giorgetta, M. A., and Coauthors, 2013: Climate and carbon cycle changes from 1850 to 2100 in MPI-ESM simulations for the Coupled Model Intercomparison Project phase 5. *J. Adv. Model. Earth Syst.,* **5,** 572–597, doi:10.1002/jame.20038.

Gregory, J. M., C. D. Jones, P. Cadule, and P. Friedlingstein, 2009: Quantifying carbon cycle feedbacks. *J. Climate,* **22,** 5232–5250, doi:10.1175/2009JCLI2949.1.

Ilyina, T., K. D. Six, J. Segschneider, E. Maier-Reimer, H. Li, and I. Núñez Riboni, 2013: Global ocean biogeochemistry model HAMOCC: Model architecture and performance as component of the MPI-Earth system model in different CMIP5 experimental realizations. *J. Adv. Model. Earth Syst.,* **5,** 287–315, doi:10.1029/2012MS000178.

Le Quéré, C., and Coauthors, 2013: The global carbon budget 1959–2011. *Earth Syst. Sci. Data,* **5,** 165–185, doi:10.5194/essd-5-165-2013.

Long, M. C., K. Lindsay, S. Peacock, J. K. Moore, and S. C. Doney, 2013: Twentieth-century oceanic carbon uptake and storage in CESM1(BGC). *J. Climate,* **26,** 6775–6800, doi:10.1175/JCLI-D-12-00184.1.

Maier-Reimer, E., U. Mikolajewicz, and A. Winguth, 1996: Future ocean uptake of CO_2: Interaction between ocean circulation and biology. *Climate Dyn.,* **12,** 711–721, doi:10.1007/s003820050138.

Matear, R., and A. Hirst, 1999: Climate change feedback on the future oceanic CO_2 uptake. *Tellus,* **51B,** 722–733, doi:10.1034/j.1600-0889.1999.t01-1-00012.x.

Millero, F. J., 1995: Thermodynamics of the carbon dioxide system in the oceans. *Geochim. Cosmochim. Acta,* **59,** 661–677, doi:10.1016/0016-7037(94)00354-O.

Moore, J. K., K. Lindsay, S. Doney, M. Long, and K. Misumi, 2013: Marine ecosystem dynamics and biogeochemical cycling in the Community Earth System Model [CESM1(BGC)]: Comparison of the 1990s with the 2090s under the RCP4.5 and RCP8.5 scenarios. *J. Climate,* **26,** 9291–9312, doi:10.1175/JCLI-D-12-00566.1.

Oschlies, A., K. G. Schulz, U. Riebesell, and A. Schmittner, 2008: Simulated 21st century's increase in oceanic suboxia by CO_2-enhanced biotic carbon export. *Global Biogeochem. Cycles,* **22,** doi:10.1029/2007GB003147.

Palmer, J., and I. Totterdell, 2001: Production and export in a global ocean ecosystem model. *Deep-Sea Res. I,* **48,** 1169–1198, doi:10.1016/S0967-0637(00)00080-7.

Plattner, G.-K., and Coauthors, 2008: Long-term climate commitments projected with climate–carbon cycle models. *J. Climate,* **21,** 2721–2751, doi:10.1175/2007JCLI1905.1.

Revelle, R., and H. Suess, 1957: Carbon dioxide exchange between atmosphere and ocean and the question of an increase of atmospheric CO_2 during the past decades. *Tellus,* **9,** 18–27, doi:10.1111/j.2153-3490.1957.tb01849.x.

Sabine, C. L., and Coauthors, 2004: The oceanic sink for anthropogenic CO_2. *Science,* **305,** 367–371, doi:10.1126/science.1097403.

Sallée, J.-B., R. J. Matear, S. R. Rintoul, and A. Lenton, 2012: Localized subduction of anthropogenic carbon dioxide in the Southern Hemisphere oceans. *Nat. Geosci.,* **5,** 579–584, doi:10.1038/ngeo1523.

——, E. Shuckburgh, N. Bruneau, A. J. S. Meijers, T. J. Bracegirdle, Z. Wang, and T. Roy, 2013: Assessment of Southern Ocean water mass circulation and characteristics in CMIP5 models: Historical bias and forcing response. *J. Geophys. Res.,* **118,** 1830–1844, doi:10.1002/jgrc.20135.

Sarmiento, J., and C. Le Quéré, 1996: Oceanic carbon dioxide uptake in a model of century-scale global warming. *Science,* **274,** 1346–1350, doi:10.1126/science.274.5291.1346.

Schneider, B., and Coauthors, 2008: Climate-induced interannual variability of marine primary and export production in three global coupled climate carbon cycle models. *Biogeosciences,* **5,** 597–614, doi:10.5194/bg-5-597-2008.

Sellers, P. J., and Coauthors, 1996: Comparison of radiative and physiological effects of doubled atmospheric CO_2 on climate. *Science,* **271,** 1402–1406, doi:10.1126/science.271.5254.1402.

Siegenthaler, U., and H. Oeschger, 1978: Predicting future atmospheric carbon-dioxide levels. *Science,* **199,** 388–395, doi:10.1126/science.199.4327.388.

Tagliabue, A., L. Bopp, and M. Gehlen, 2011: The response of marine carbon and nutrient cycles to ocean acidification: Large uncertainties related to phytoplankton physiological assumptions. *Global Biogeochem. Cycles,* **25,** GB3017, doi:10.1029/2010GB003929.

Takahashi, T., and Coauthors, 2009: Climatological mean and decadal change in surface ocean pCO_2, and net sea-air CO_2 flux

over the global oceans. *Deep-Sea Res. II,* **56,** 554–577, doi:10.1016/j.dsr2.2008.12.009.

Taylor, K. E., R. J. Stouffer, and G. A. Meehl, 2012: An overview of CMIP5 and the experiment design. *Bull. Amer. Meteor. Soc.,* **93,** 485–498, doi:10.1175/BAMS-D-11-00094.1.

Tjiputra, J. F., K. Assmann, and C. Heinze, 2010: Anthropogenic carbon dynamics in the changing ocean. *Ocean Sci.,* **6,** 605–614, doi:10.5194/os-6-605-2010.

——, C. Roelandt, M. Bentsen, D. M. Lawrence, T. Lorentzen, J. Schwinger, O. Seland, and C. Heinze, 2013: Evaluation of the carbon cycle components in the Norwegian Earth System Model (NorESM). *Geosci. Model Dev.,* **6,** 301–325, doi:10.5194/gmd-6-301-2013.

Voldoire, A., and Coauthors, 2013: The CNRM-CM5.1 global climate model: Description and basic evaluation. *Climate Dyn.,* **40** (9–10), 2091–2121, doi:10.1007/s00382-011-1259-y.

Weiss, R., 1970: Solubility of nitrogen, oxygen and argon in water and seawater. *Deep-Sea Res. Oceanogr. Abstr.,* **17,** 721–735, doi:10.1016/0011-7471(70)90037-9.

——, 1974: Carbon dioxide in water and seawater: The solubility of a non-ideal gas. *Mar. Chem.,* **2,** 203–215, doi:10.1016/0304-4203(74)90015-2.

Zahariev, K., J. R. Christian, and K. L. Denman, 2008: Preindustrial, historical, and fertilization simulations using a global ocean carbon model with new parameterizations of iron limitation, calcification, and N-2 fixation. *Prog. Oceanogr.,* **77,** 56–82, doi:10.1016/j.pocean.2008.01.007.

Zeebe, R. E., and D. A. Wolf-Gladrow, 2001: *CO_2 in Seawater: Equilibrium, Kinetics, Isotopes*. Elsevier Science, 360 pp.

Zickfeld, K., M. Eby, H. D. Matthews, A. Schmittner, and A. J. Weaver, 2011: Nonlinearity of carbon cycle feedbacks. *J. Climate,* **24,** 4255–4275, doi:10.1175/2011JCLI3898.1.